2010

All-sky search for gravitational-wave bursts in the first joint LIGO-GEO-Virgo run

Matthew Benacquista
The University of Texas Rio Grande Valley

Teviet Creighton
The University of Texas Rio Grande Valley

Mario C. Diaz
The University of Texas Rio Grande Valley

R. Grosso

Soumya Mohanty
The University of Texas Rio Grande Valley

See next page for additional authors

All-sky search for gravitational-wave bursts in the first joint LIGO-GEO-Virgo run

J. Abadie,[29] B. P. Abbott,[29] R. Abbott,[29] T. Accadia,[27] F. Acernese,[19a,19c] R. Adhikari,[29] P. Ajith,[29] B. Allen,[2,77] G. Allen,[52] E. Amador Ceron,[77] R. S. Amin,[34] S. B. Anderson,[29] W. G. Anderson,[77] F. Antonucci,[22a] M. A. Arain,[64] M. Araya,[29] K. G. Arun,[26] Y. Aso,[29] S. Aston,[63] P. Astone,[22a] P. Aufmuth,[28] C. Aulbert,[2] S. Babak,[1] P. Baker,[37] G. Ballardin,[12] S. Ballmer,[29] D. Barker,[30] F. Barone,[19a,19c] B. Barr,[65] P. Barriga,[76] L. Barsotti,[32] M. Barsuglia,[4] M. A. Barton,[30] I. Bartos,[11] R. Bassiri,[65] M. Bastarrika,[65] Th. S. Bauer,[41a] B. Behnke,[1] M. G. Beker,[41a] A. Belletoile,[27] M. Benacquista,[59] J. Betzwieser,[29] P. T. Beyersdorf,[48] S. Bigotta,[21a,21b] I. A. Bilenko,[38] G. Billingsley,[29] S. Birindelli,[43a] R. Biswas,[77] M. A. Bizouard,[26] E. Black,[29] J. K. Blackburn,[29] L. Blackburn,[32] D. Blair,[76] B. Bland,[30] M. Blom,[41a] C. Boccara,[15] O. Bock,[2] T. P. Bodiya,[32] R. Bondarescu,[54] F. Bondu,[43b] L. Bonelli,[21a,21b] R. Bonnand,[33] R. Bork,[29] M. Born,[2] S. Bose,[78] L. Bosi,[20a] B. Bouhou,[4] S. Braccini,[21a] C. Bradaschia,[21a] P. R. Brady,[77] V. B. Braginsky,[38] J. E. Brau,[70] J. Breyer,[2] D. O. Bridges,[31] A. Brillet,[43a] M. Brinkmann,[2] V. Brisson,[26] M. Britzger,[2] A. F. Brooks,[29] D. A. Brown,[53] R. Budzyński,[45b] T. Bulik,[45c,45d] A. Bullington,[52] H. J. Bulten,[41a,41b] A. Buonanno,[66] O. Burmeister,[2] D. Buskulic,[27] C. Buy,[4] R. L. Byer,[52] L. Cadonati,[67] G. Cagnoli,[17a] J. Cain,[56] E. Calloni,[19a,19b] J. B. Camp,[39] E. Campagna,[17a,17b] J. Cannizzo,[39] K. C. Cannon,[29] B. Canuel,[12] J. Cao,[32] C. D. Capano,[53] F. Carbognani,[12] L. Cardenas,[29] S. Caudill,[34] M. Cavaglià,[56] F. Cavalier,[26] R. Cavalieri,[12] G. Cella,[21a] C. Cepeda,[29] E. Cesarini,[17b] T. Chalermsongsak,[29] E. Chalkley,[65] P. Charlton,[10] E. Chassande-Mottin,[4] S. Chatterji,[29] S. Chelkowski,[63] Y. Chen,[7] A. Chincarini,[18] N. Christensen,[9] S. S. Y. Chua,[5] C. T. Y. Chung,[55] D. Clark,[52] J. Clark,[8] J. H. Clayton,[77] F. Cleva,[43a] E. Coccia,[23a,23b] C. N. Colacino,[21a] J. Colas,[12] A. Colla,[22a,22b] M. Colombini,[22b] R. Conte,[72] D. Cook,[30] T. R. C. Corbitt,[32] N. Cornish,[37] A. Corsi,[22a] J.-P. Coulon,[43a] D. Coward,[76] D. C. Coyne,[29] J. D. E. Creighton,[77] T. D. Creighton,[59] A. M. Cruise,[63] R. M. Culter,[63] A. Cumming,[65] L. Cunningham,[65] E. Cuoco,[12] K. Dahl,[2] S. L. Danilishin,[38] S. D'Antonio,[23a] K. Danzmann,[2,28] V. Dattilo,[12] B. Daudert,[29] M. Davier,[26] G. Davies,[8] E. J. Daw,[57] R. Day,[12] T. Dayanga,[78] R. De Rosa,[19a,19b] D. DeBra,[52] J. Degallaix,[2] M. del Prete,[21a,21c] V. Dergachev,[68] R. DeSalvo,[29] S. Dhurandhar,[25] L. Di Fiore,[19a] A. Di Lieto,[21a,21b] M. Di Paolo Emilio,[23a,23c] A. Di Virgilio,[21a] M. Díaz,[59] A. Dietz,[27] F. Donovan,[32] K. L. Dooley,[64] E. E. Doomes,[51] M. Drago,[44c,44d] R. W. P. Drever,[6] J. Driggers,[29] J. Dueck,[2] I. Duke,[32] J.-C. Dumas,[76] S. Dwyer,[32] M. Edgar,[65] M. Edwards,[8] A. Effler,[30] P. Ehrens,[29] T. Etzel,[29] M. Evans,[32] T. Evans,[31] V. Fafone,[23a,23b] S. Fairhurst,[8] Y. Faltas,[64] Y. Fan,[76] D. Fazi,[29] H. Fehrmann,[2] I. Ferrante,[21a,21b] F. Fidecaro,[21a,21b] L. S. Finn,[54] I. Fiori,[12] R. Flaminio,[33] K. Flasch,[77] S. Foley,[32] C. Forrest,[71] N. Fotopoulos,[77] J.-D. Fournier,[43a] J. Franc,[33] S. Frasca,[22a,22b] F. Frasconi,[21a] M. Frede,[2] M. Frei,[58] Z. Frei,[14] A. Freise,[63] R. Frey,[70] T. T. Fricke,[34] D. Friedrich,[2] P. Fritschel,[32] V. V. Frolov,[31] P. Fulda,[63] M. Fyffe,[31] M. Galimberti,[33] L. Gammaitoni,[20a,20b] J. A. Garofoli,[53] F. Garufi,[19a,19b] G. Gemme,[18] E. Genin,[12] A. Gennai,[21a] S. Ghosh,[78] J. A. Giaime,[34,31] S. Giampanis,[2] K. D. Giardina,[31] A. Giazotto,[21a] E. Goetz,[68] L. M. Goggin,[77] G. González,[34] S. Goßler,[2] R. Gouaty,[27] M. Granata,[4] A. Grant,[65] S. Gras,[76] C. Gray,[30] R. J. S. Greenhalgh,[47] A. M. Gretarsson,[13] C. Greverie,[43a] R. Grosso,[59] H. Grote,[2] S. Grunewald,[1] G. M. Guidi,[17a,17b] E. K. Gustafson,[29] R. Gustafson,[68] B. Hage,[28] J. M. Hallam,[63] D. Hammer,[77] G. D. Hammond,[65] C. Hanna,[29] J. Hanson,[31] J. Harms,[69] G. M. Harry,[32] I. W. Harry,[8] E. D. Harstad,[70] K. Haughian,[65] K. Hayama,[2] J.-F. Hayau,[43b] T. Hayler,[47] J. Heefner,[29] H. Heitmann,[43a] P. Hello,[26] I. S. Heng,[65] A. Heptonstall,[29] M. Hewitson,[2] S. Hild,[65] E. Hirose,[53] D. Hoak,[31] K. A. Hodge,[29] K. Holt,[31] D. J. Hosken,[62] J. Hough,[65] E. Howell,[76] D. Hoyland,[63] D. Huet,[12] B. Hughey,[32] S. Husa,[61] S. H. Huttner,[65] D. R. Ingram,[30] T. Isogai,[9] A. Ivanov,[29] P. Jaranowski,[45e] W. W. Johnson,[34] D. I. Jones,[74] G. Jones,[8] R. Jones,[65] L. Ju,[76] P. Kalmus,[29] V. Kalogera,[42] S. Kandhasamy,[69] J. Kanner,[66] E. Katsavounidis,[32] K. Kawabe,[30] S. Kawamura,[40] F. Kawazoe,[2] W. Kells,[29] D. G. Keppel,[29] A. Khalaidovski,[2] F. Y. Khalili,[38] R. Khan,[11] E. Khazanov,[24] H. Kim,[2] P. J. King,[29] J. S. Kissel,[34] S. Klimenko,[64] K. Kokeyama,[40] V. Kondrashov,[29] R. Kopparapu,[54] S. Koranda,[77] I. Kowalska,[45c] D. Kozak,[29] V. Kringel,[2] B. Krishnan,[1] A. Królak,[45a,45f] G. Kuehn,[2] J. Kullman,[2] R. Kumar,[65] P. Kwee,[28] P. K. Lam,[5] M. Landry,[30] M. Lang,[54] B. Lantz,[52] N. Lastzka,[2] A. Lazzarini,[29] P. Leaci,[2] M. Lei,[29] N. Leindecker,[52] I. Leonor,[70] N. Leroy,[26] N. Letendre,[27] T. G. F. Li,[41a] H. Lin,[64] P. E. Lindquist,[29] T. B. Littenberg,[37] N. A. Lockerbie,[75] D. Lodhia,[63] M. Lorenzini,[17a] V. Loriette,[15] M. Lormand,[31] G. Losurdo,[17a] P. Lu,[52] M. Lubinski,[30] A. Lucianetti,[64] H. Lück,[2,28] A. Lundgren,[53] B. Machenschalk,[2] M. MacInnis,[32] M. Mageswaran,[29] K. Mailand,[29] E. Majorana,[22a] C. Mak,[29] I. Maksimovic,[15] N. Man,[43a] I. Mandel,[42] V. Mandic,[69] M. Mantovani,[21c] F. Marchesoni,[20a] F. Marion,[27] S. Márka,[11] Z. Márka,[11] A. Markosyan,[52] J. Markowitz,[32] E. Maros,[29] J. Marque,[12] F. Martelli,[17a,17b] I. W. Martin,[65] R. M. Martin,[64] J. N. Marx,[29] K. Mason,[32] A. Masserot,[27] F. Matichard,[34,32] L. Matone,[11] R. A. Matzner,[58] N. Mavalvala,[32] R. McCarthy,[30] D. E. McClelland,[5] S. C. McGuire,[51] G. McIntyre,[29] D. J. A. McKechan,[8] M. Mehmet,[2] A. Melatos,[55] A. C. Melissinos,[71] G. Mendell,[30] D. F. Menéndez,[54] R. A. Mercer,[77] L. Merill,[76] S. Meshkov,[29] C. Messenger,[2] M. S. Meyer,[31] H. Miao,[76] C. Michel,[33] L. Milano,[19a,19b]

J. Miller,[65] Y. Minenkov,[23a] Y. Mino,[7] S. Mitra,[29] V. P. Mitrofanov,[38] G. Mitselmakher,[64] R. Mittleman,[32] O. Miyakawa,[29] B. Moe,[77] M. Mohan,[12] S. D. Mohanty,[59] S. R. P. Mohapatra,[67] J. Moreau,[15] G. Moreno,[30] N. Morgado,[33] A. Morgia,[23a,23b] K. Mors,[2] S. Mosca,[19a,19b] V. Moscatelli,[22a] K. Mossavi,[2] B. Mours,[27] C. MowLowry,[5] G. Mueller,[64] S. Mukherjee,[59] A. Mullavey,[5] H. Müller-Ebhardt,[2] J. Munch,[62] P. G. Murray,[65] T. Nash,[29] R. Nawrodt,[65] J. Nelson,[65] I. Neri,[20a,20b] G. Newton,[65] E. Nishida,[40] A. Nishizawa,[40] F. Nocera,[12] E. Ochsner,[66] J. O'Dell,[47] G. H. Ogin,[29] R. Oldenburg,[77] B. O'Reilly,[31] R. O'Shaughnessy,[54] D. J. Ottaway,[62] R. S. Ottens,[64] H. Overmier,[31] B. J. Owen,[54] A. Page,[63] G. Pagliaroli,[23a,23c] L. Palladino,[23a,23c] C. Palomba,[22a] Y. Pan,[66] C. Pankow,[64] F. Paoletti,[21a,12] M. A. Papa,[1,77] S. Pardi,[19a,19b] M. Parisi,[19b] A. Pasqualetti,[12] R. Passaquieti,[21a,21b] D. Passuello,[21a] P. Patel,[29] D. Pathak,[8] M. Pedraza,[29] L. Pekowsky,[53] S. Penn,[16] C. Peralta,[1] A. Perreca,[63] G. Persichetti,[19a,19b] M. Pichot,[43a] M. Pickenpack,[2] F. Piergiovanni,[17a,17b] M. Pietka,[45e] L. Pinard,[33] I. M. Pinto,[73] M. Pitkin,[65] H. J. Pletsch,[2] M. V. Plissi,[65] R. Poggiani,[21a,21b] F. Postiglione,[72] M. Prato,[18] M. Principe,[73] R. Prix,[2] G. A. Prodi,[44a,44b] L. Prokhorov,[38] O. Puncken,[2] M. Punturo,[20a] P. Puppo,[22a] V. Quetschke,[64] F. J. Raab,[30] D. S. Rabeling,[5] D. S. Rabeling,[41a,41b] H. Radkins,[30] P. Raffai,[14] Z. Raics,[11] M. Rakhmanov,[59] P. Rapagnani,[22a,22b] V. Raymond,[42] V. Re,[44a,44b] C. M. Reed,[30] T. Reed,[35] T. Regimbau,[43a] H. Rehbein,[2] S. Reid,[65] D. H. Reitze,[64] F. Ricci,[22a,22b] R. Riesen,[31] K. Riles,[68] P. Roberts,[3] N. A. Robertson,[29,65] F. Robinet,[26] C. Robinson,[8] E. L. Robinson,[1] A. Rocchi,[23a] S. Roddy,[31] C. Röver,[2] L. Rolland,[27] J. Rollins,[11] J. D. Romano,[59] R. Romano,[19a,19c] J. H. Romie,[31] D. Rosińska,[45g] S. Rowan,[65] A. Rüdiger,[2] P. Ruggi,[12] K. Ryan,[30] S. Sakata,[40] F. Salemi,[2] L. Sammut,[55] L. Sancho de la Jordana,[61] V. Sandberg,[30] V. Sannibale,[29] L. Santamaría,[1] G. Santostasi,[36] S. Saraf,[49] P. Sarin,[32] B. Sassolas,[33] B. S. Sathyaprakash,[8] S. Sato,[40] M. Satterthwaite,[5] P. R. Saulson,[53] R. Savage,[30] R. Schilling,[2] R. Schnabel,[2] R. Schofield,[70] B. Schulz,[2] B. F. Schutz,[1,8] P. Schwinberg,[30] J. Scott,[65] S. M. Scott,[5] A. C. Searle,[29] F. Seifert,[2,29] D. Sellers,[31] A. S. Sengupta,[29] D. Sentenac,[12] A. Sergeev,[24] B. Shapiro,[32] P. Shawhan,[66] D. H. Shoemaker,[32] A. Sibley,[31] X. Siemens,[77] D. Sigg,[30] A. M. Sintes,[61] G. Skelton,[77] B. J. J. Slagmolen,[5] J. Slutsky,[34] J. R. Smith,[53] M. R. Smith,[29] N. D. Smith,[32] K. Somiya,[7] B. Sorazu,[65] L. Sperandio,[23a,23b] A. J. Stein,[32] L. C. Stein,[32] S. Steplewski,[78] A. Stochino,[29] R. Stone,[59] K. A. Strain,[65] S. Strigin,[38] A. Stroeer,[39] R. Sturani,[17a,17b] A. L. Stuver,[31] T. Z. Summerscales,[3] M. Sung,[34] S. Susmithan,[76] P. J. Sutton,[8] B. Swinkels,[12] G. P. Szokoly,[14] D. Talukder,[78] D. B. Tanner,[64] S. P. Tarabrin,[38] J. R. Taylor,[2] R. Taylor,[29] K. A. Thorne,[31] K. S. Thorne,[7] A. Thüring,[28] C. Titsler,[54] K. V. Tokmakov,[65,75] A. Toncelli,[21a,21b] M. Tonelli,[21a,21b] C. Torres,[31] C. I. Torrie,[29,65] E. Tournefier,[27] F. Travasso,[20a,20b] G. Traylor,[31] M. Trias,[61] J. Trummer,[27] L. Turner,[29] D. Ugolini,[60] K. Urbanek,[52] H. Vahlbruch,[28] G. Vajente,[21a,21b] M. Vallisneri,[7] J. F. J. van den Brand,[41a,41b] C. Van Den Broeck,[8] S. van der Putten,[41a] M. V. van der Sluys,[42] S. Vass,[29] R. Vaulin,[77] M. Vavoulidis,[26] A. Vecchio,[63] G. Vedovato,[44c] A. A. van Veggel,[65] J. Veitch,[63] P. J. Veitch,[62] C. Veltkamp,[2] D. Verkindt,[27] F. Vetrano,[17a,17b] A. Viceré,[17a,17b] A. Villar,[29] J.-Y. Vinet,[43a] H. Vocca,[20a] C. Vorvick,[30] S. P. Vyachanin,[38] S. J. Waldman,[32] L. Wallace,[29] A. Wanner,[2] R. L. Ward,[29] M. Was,[26] P. Wei,[53] M. Weinert,[2] A. J. Weinstein,[29] R. Weiss,[32] L. Wen,[7,76] S. Wen,[34] P. Wessels,[2] M. West,[53] T. Westphal,[2] K. Wette,[5] J. T. Whelan,[46] S. E. Whitcomb,[29] B. F. Whiting,[64] C. Wilkinson,[30] P. A. Willems,[29] H. R. Williams,[54] L. Williams,[64] B. Willke,[2,28] I. Wilmut,[47] L. Winkelmann,[2] W. Winkler,[2] C. C. Wipf,[32] A. G. Wiseman,[77] G. Woan,[65] R. Wooley,[31] J. Worden,[30] I. Yakushin,[31] H. Yamamoto,[29] K. Yamamoto,[2] D. Yeaton-Massey,[29] S. Yoshida,[50] M. Yvert,[27] M. Zanolin,[13] L. Zhang,[29] Z. Zhang,[76] C. Zhao,[76] N. Zotov,[35] M. E. Zucker,[32] and J. Zweizig[29]

(The LIGO Scientific Collaboration and The Virgo Collaboration)

[1]*Albert-Einstein-Institut, Max-Planck-Institut für Gravitationsphysik, D-14476 Golm, Germany*[*]
[2]*Albert-Einstein-Institut, Max-Planck-Institut für Gravitationsphysik, D-30167 Hannover, Germany*[*]
[3]*Andrews University, Berrien Springs, Michigan 49104, USA*[*]
[4]*AstroParticule et Cosmologie (APC), CNRS: UMR7164-IN2P3-Observatoire de Paris-Université Denis Diderot-Paris 7 - CEA : DSM/IRFU, France*[†]
[5]*Australian National University, Canberra, 0200, Australia*[*]
[6]*California Institute of Technology, Pasadena, California 91125, USA*[*]
[7]*Caltech-CaRT, Pasadena, California 91125, USA*[*]
[8]*Cardiff University, Cardiff, CF24 3AA, United Kingdom*[*]
[9]*Carleton College, Northfield, Minnesota 55057, USA*[*]
[10]*Charles Sturt University, Wagga Wagga, NSW 2678, Australia*[*]
[11]*Columbia University, New York, New York 10027, USA*[*]
[12]*European Gravitational Observatory (EGO), I-56021 Cascina (PI), Italy*[†]
[13]*Embry-Riddle Aeronautical University, Prescott, Arizona 86301 USA*[*]

[14]Eötvös University, ELTE 1053 Budapest, Hungary*
[15]ESPCI, CNRS, F-75005 Paris, France†
[16]Hobart and William Smith Colleges, Geneva, New York 14456, USA*
[17a]INFN, Sezione di Firenze, I-50019 Sesto Fiorentino, Italy†
[17b]Università degli Studi di Urbino 'Carlo Bo', I-61029 Urbino, Italy†
[18]INFN, Sezione di Genova; I-16146 Genova, Italy†
[19a]INFN, Sezione di Napoli, I-80126 Napoli, Italy†
[19b]Università di Napoli 'Federico II' Complesso Universitario di Monte S.Angelo, I-80126 Napoli, Italy†
[19c]Università di Salerno, Fisciano, I-84084 Salerno, Italy†
[20a]INFN, Sezione di Perugia, I-06123 Perugia, Italy†
[20b]Università di Perugia, I-06123 Perugia, Italy†
[21a]INFN, Sezione di Pisa, I-56127 Pisa, Italy†
[21b]Università di Pisa, I-56127 Pisa, Italy†
[21c]Università di Siena, I-53100 Siena, Italy†
[22a]INFN, Sezione di Roma, I-00185 Roma, Italy†
[22b]Università 'La Sapienza', I-00185 Roma, Italy†
[23a]INFN, Sezione di Roma Tor Vergata, I-00133 Roma, Italy†
[23b]Università di Roma Tor Vergata, I-00133 Roma, Italy†
[23c]Università dell'Aquila, I-67100 L'Aquila, Italy†
[24]Institute of Applied Physics, Nizhny Novgorod, 603950, Russia*
[25]Inter-University Centre for Astronomy and Astrophysics, Pune - 411007, India*
[26]LAL, Université Paris-Sud, IN2P3/CNRS, F-91898 Orsay, France†
[27]Laboratoire d'Annecy-le-Vieux de Physique des Particules (LAPP), IN2P3/CNRS, Université de Savoie, F-74941 Annecy-le-Vieux, France†
[28]Leibniz Universität Hannover, D-30167 Hannover, Germany*
[29]LIGO - California Institute of Technology, Pasadena, California 91125, USA*
[30]LIGO - Hanford Observatory, Richland, Washington 99352, USA*
[31]LIGO - Livingston Observatory, Livingston, Louisiana 70754, USA*
[32]LIGO - Massachusetts Institute of Technology, Cambridge, Massachusetts 02139, USA*
[33]Laboratoire des Matériaux Avancés (LMA), IN2P3/CNRS, F-69622 Villeurbanne, Lyon, France†
[34]Louisiana State University, Baton Rouge, Louisiana 70803, USA*
[35]Louisiana Tech University, Ruston, Louisiana 71272, USA*
[36]McNeese State University, Lake Charles, Louisiana 70609 USA*
[37]Montana State University, Bozeman, Montana 59717, USA*
[38]Moscow State University, Moscow, 119992, Russia*
[39]NASA/Goddard Space Flight Center, Greenbelt, Maryland 20771, USA*
[40]National Astronomical Observatory of Japan, Tokyo 181-8588, Japan*
[41a]Nikhef, National Institute for Subatomic Physics, P.O. Box 41882, 1009 DB Amsterdam, The Netherlands†
[41b]VU University Amsterdam, De Boelelaan 1081, 1081 HV Amsterdam, The Netherlands†
[42]Northwestern University, Evanston, Illinois 60208, USA*
[43a]Université Nice-Sophia-Antipolis, CNRS, Observatoire de la Côte d'Azur, F-06304 Nice, France†
[43b]Institut de Physique de Rennes, CNRS, Université de Rennes 1, 35042 Rennes, France†
[44a]INFN, Gruppo Collegato di Trento, Trento, Italy†
[44b]Università di Trento, I-38050 Povo, Trento, Italy†
[44c]INFN, Sezione di Padova, I-35131 Padova, Italy†
[44d]Università di Padova, I-35131 Padova, Italy†
[45a]IM-PAN, 00-956 Warsaw, Poland†
[45b]Warsaw University, 00-681 Warsaw, Poland†
[45c]Astronomical Observatory of Warsaw University, 00-478 Warsaw, Poland†
[45d]CAMK-PAN, 00-716 Warsaw, Poland†
[45e]Białystok University, 15-424 Białystok, Poland†
[45f]IPJ, 05-400 Świerk-Otwock, Poland†
[45g]Institute of Astronomy, 65-265 Zielona Góra, Poland†
[46]Rochester Institute of Technology, Rochester, New York 14623, USA*
[47]Rutherford Appleton Laboratory, HSIC, Chilton, Didcot, Oxon OX11 0QX United Kingdom*
[48]San Jose State University, San Jose, California 95192, USA*
[49]Sonoma State University, Rohnert Park, California 94928, USA*
[50]Southeastern Louisiana University, Hammond, Louisiana 70402, USA*
[51]Southern University and A&M College, Baton Rouge, Louisiana 70813, USA*
[52]Stanford University, Stanford, California 94305, USA*
[53]Syracuse University, Syracuse, New York 13244, USA*

[54]*The Pennsylvania State University, University Park, Pennsylvania 16802, USA**
[55]*The University of Melbourne, Parkville VIC 3010, Australia**
[56]*The University of Mississippi, University, Mississippi 38677, USA**
[57]*The University of Sheffield, Sheffield S10 2TN, United Kingdom, USA**
[58]*The University of Texas at Austin, Austin, Texas 78712, USA**
[59]*The University of Texas at Brownsville and Texas Southmost College, Brownsville, Texas 78520, USA**
[60]*Trinity University, San Antonio, Texas 78212, USA**
[61]*Universitat de les Illes Balears, E-07122 Palma de Mallorca, Spain**
[62]*University of Adelaide, Adelaide, SA 5005, Australia**
[63]*University of Birmingham, Birmingham, B15 2TT, United Kingdom**
[64]*University of Florida, Gainesville, Florida 32611, USA**
[65]*University of Glasgow, Glasgow, G12 8QQ, United Kingdom**
[66]*University of Maryland, College Park, Maryland 20742 USA**
[67]*University of Massachusetts - Amherst, Amherst, Massachusetts 01003, USA**
[68]*University of Michigan, Ann Arbor, Michigan 48109, USA**
[69]*University of Minnesota, Minneapolis, Minnesota 55455, USA**
[70]*University of Oregon, Eugene, Oregon 97403, USA**
[71]*University of Rochester, Rochester, New York 14627, USA**
[72]*University of Salerno, I-84084 Fisciano (Salerno), Italy** *and INFN*
[73]*University of Sannio at Benevento, I-82100 Benevento, Italy** *and INFN*
[74]*University of Southampton, Southampton, SO17 1BJ, United Kingdom**
[75]*University of Strathclyde, Glasgow, G1 1XQ, United Kingdom**
[76]*University of Western Australia, Crawley, Washington 6009, Australia, USA**
[77]*University of Wisconsin–Milwaukee, Milwaukee, Wisconsin 53201, USA**
[78]*Washington State University, Pullman, Washington 99164, USA**
(Received 4 March 2010; published 5 May 2010; corrected 12 April 2012)

We present results from an all-sky search for unmodeled gravitational-wave bursts in the data collected by the LIGO, GEO 600 and Virgo detectors between November 2006 and October 2007. The search is performed by three different analysis algorithms over the frequency band 50–6000 Hz. Data are analyzed for times with at least two of the four LIGO-Virgo detectors in coincident operation, with a total live time of 266 days. No events produced by the search algorithms survive the selection cuts. We set a frequentist upper limit on the rate of gravitational-wave bursts impinging on our network of detectors. When combined with the previous LIGO search of the data collected between November 2005 and November 2006, the upper limit on the rate of detectable gravitational-wave bursts in the 64–2048 Hz band is 2.0 events per year at 90% confidence. We also present event rate versus strength exclusion plots for several types of plausible burst waveforms. The sensitivity of the combined search is expressed in terms of the root-sum-squared strain amplitude for a variety of simulated waveforms and lies in the range 6×10^{-22} $\mathrm{Hz}^{-1/2}$ to 2×10^{-20} $\mathrm{Hz}^{-1/2}$. This is the first untriggered burst search to use data from the LIGO and Virgo detectors together, and the most sensitive untriggered burst search performed so far.

DOI: 10.1103/PhysRevD.81.102001 PACS numbers: 04.80.Nn, 07.05.Kf, 95.30.Sf, 95.85.Sz

I. INTRODUCTION

The LIGO Scientific Collaboration (LSC) and the Virgo Collaboration operate a network of interferometric gravitational-wave (GW) detectors with the goal of detecting gravitational waves from astrophysical sources. Some of these sources may produce transient ''bursts'' of GW radiation with relatively short duration ($\lesssim 1$ s). Plausible burst sources [1] include merging compact binary systems consisting of black holes and/or neutron stars [2,3], core-collapse supernovae [4], neutron star collapse [5], star-quakes associated with magnetar flares [6] or pulsar glitches [7], cosmic string cusps [8], and other violent events in the Universe.

During the most recent data-taking run five GW detectors were operational. The three LIGO detectors [9] started their Science Run 5 (S5) in November 2005, and the GEO 600 detector [10] joined the S5 run in January 2006. The Virgo detector [11] began its Virgo Science Run 1 (VSR1) in May 2007. All five instruments took data together until the beginning of October 2007.

An all-sky search for GW burst signals has already been conducted on the first calendar year of the LIGO S5 data (referred to as ''S5y1'') in a wide frequency band of 64–6000 Hz [12,13]. In this paper, we report on a search for GW burst signals in the frequency band 50–6000 Hz for the rest of the S5/VSR1 run, referred to as ''S5y2/VSR1.'' It

*The LIGO Scientific Collaboration.
†The Virgo Collaboration.

includes data collected by the LIGO and Virgo detectors, which had comparable sensitivities, and uses three different search algorithms. In comparison with the S5y1 analysis, the network of LIGO and Virgo detectors, spread over three sites, provides better sky coverage as well as improved capabilities to reject spurious signals. S5y2/VSR1 is also the first long-term observation with the worldwide network of interferometric detectors. This is a major step forward with respect to previous observations led by the network of resonant detectors [14,15], since, as we will show in this paper, the performance is improved by more than 1 order of magnitude both in the analyzed frequency bandwidth and the level of instrumental noise.

This paper is organized as follows. In Sec. II we describe the LSC and Virgo instruments. In Sec. III we give a brief overview of the search procedure. In Sec. IV we present the search algorithms. Simulations are described in Sec. V, and the error analysis in Sec. VI. The results of the search are presented in Sec. VII, and astrophysical implications are discussed in Sec. VIII. The appendices provide additional details on data characterization and the analysis pipelines.

II. DETECTORS

A. LIGO

LIGO consists of three detectors at two observatories in the United States. Each detector is a large Michelson-type interferometer with additional mirrors forming Fabry-Perot cavities in the arms and a power-recycling mirror in the input beam path. Interferometric sensing and feedback is used to ''lock'' the mirror positions and orientations to keep all of the optical cavities on resonance. A gravitational wave is sensed as a quadrupolar strain, measured interferometrically as an effective difference between the lengths of the two arms. The LIGO Hanford Observatory, in Washington, houses independent detectors with the arm lengths of 4 km and 2 km, called H1 and H2, respectively. The LIGO Livingston Observatory, in Louisiana, has a single detector with 4-km arms, called L1. The detector instrumentation and operation are described in detail elsewhere [9], and the improvements leading up to the S5 run which are most relevant for GW burst searches have been described in the first-year search [12].

The best achieved sensitivities of the LIGO detectors during the second year of S5, as a function of signal frequency, are shown in Fig. 1. The detectors are most sensitive over a band extending from about 40 Hz to a few kHz. Seismic noise dominates at lower frequencies since the effectiveness of the seismic isolation system is a very strong function of frequency. Above ~200 Hz, laser shot noise corrected for the Fabry-Perot cavity response yields an effective strain noise that rises linearly with frequency. The sensitivity at intermediate frequencies is determined mainly by thermal noise, with contributions from other sources. The peaks at ~350 Hz and harmonics are the thermally-excited vibrational modes of the wires from

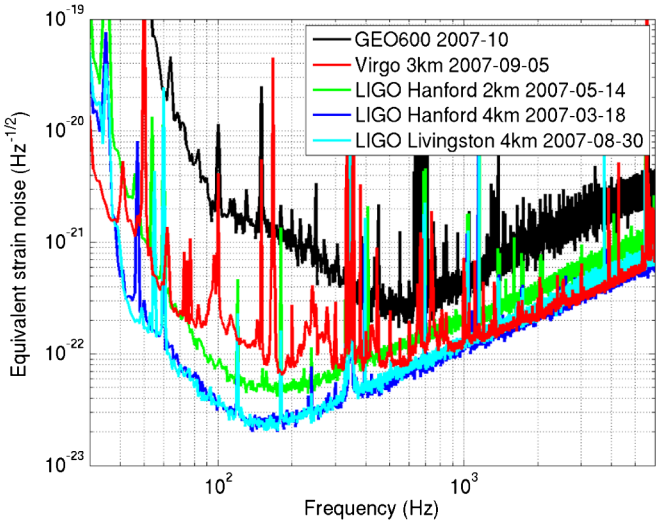

FIG. 1 (color online). Best noise amplitude spectral densities of the five LSC/Virgo detectors during S5/VSR1.

which the large mirrors are suspended. Smaller peaks are due to other mechanical resonances, power line harmonics, and calibration signals.

Commissioning periods during the second year of S5 led to incremental improvements in the detector sensitivities. The most significant of these were in January 2007, when the seismic isolation systems at both sites were improved to reduce the coupling of microseismic noise to the mirror suspensions, thereby mitigating noise from the nonlinear Barkhausen effect [16] in the magnets used to control the mirror positions; and in August 2007, when the L1 frequency stabilization servo was retuned. Overall, the average sensitivities of the H1 and L1 detectors during the second year were about 20% better than the first-year averages, while the H2 detector (less sensitive to begin with by a factor of ~2) had about the same average sensitivity in both years. The operational duty cycles for all three detectors also improved as the run progressed, from (72.8%, 76.7%, 61.0%) averaged over the first year to (84.0%, 80.6%, 73.6%) averaged over the second year for H1, H2, and L1, respectively.

B. GEO 600

The GEO 600 detector, located near Hannover, Germany, also operated during S5, though with a lower sensitivity than the LIGO and Virgo detectors. The GEO 600 data are not used in the initial search stage of the current study as the modest gains in the sensitivity to GW signals would not offset the increased complexity of the analysis. The GEO 600 data are held in reserve, and used to follow up any detection candidates from the LIGO-Virgo analysis.

GEO 600 began its participation in S5 on January 21 2006, acquiring data during nights and weekends.

Commissioning work was performed during the daytime, focussing on gaining a better understanding of the detector and improving data quality. GEO switched to full-time data taking from May 1 to October 6, 2006, then returned to night-and-weekend mode through the end of the S5 run. Overall GEO 600 collected about 415 days of science data during S5, for a duty cycle of 59.7% over the full S5 run.

C. Virgo

The Virgo detector [11], also called V1, is an interferometer with 3 km arms located near Pisa in Italy. One of the main instrumental differences with respect to LIGO is the seismic isolation system based on superattenuators [17], chains of passive attenuators capable of filtering seismic disturbances in 6 degrees of freedom with sub-Hertz corner frequencies. For VSR1, the Virgo duty cycle was 81% and the longest continuous period with the mirror positions interferometrically controlled was more than 94 hours. Another benefit from superattenuators is a significant reduction of the detector noise at very low-frequency (< 40 Hz) where Virgo surpasses the LIGO sensitivity.

Above 300 Hz, the spectral sensitivity achieved by Virgo during VSR1 is comparable to that of LIGO (see Fig. 1). Above 500 Hz the Virgo sensitivity is dominated by shot noise. Below 500 Hz there is excess noise due to environmental and instrumental noise sources, and below 300 Hz these produce burstlike transients.

Because of the different orientation of its arms, the antenna pattern (angular sensitivity) of Virgo is complementary to that of the LIGO detectors, with highest response in directions of low LIGO sensitivity. Virgo therefore significantly increases the sky coverage of the network. In addition, simultaneous observations with the three LIGO-Virgo sites improve rejection of spurious signals and allow reconstruction of the sky position and waveforms of detected GW sources.

III. SEARCH OVERVIEW

The analysis described in this paper uses data from the LIGO detectors collected from 14 November 2006 through 1 October 2007 (S5y2), and Virgo data from VSR1, which started on 18 May 18 2007 and ended at the same time as S5 [18]. The procedure used for this S5y2/VSR1 search is the same as that used for S5y1 [12]. In this section we briefly review the main stages of the analysis.

A. Data quality flags

The detectors are occasionally affected by instrumental or data acquisition artifacts as well as by periods of degraded sensitivity or an excessive rate of transient noise due to environmental conditions such as bad weather. Low-quality data segments are tagged with data quality flags (DQFs). These DQFs are divided into three categories depending on their seriousness. Category 1 DQFs are used to define the data segments processed by the analysis algorithms. Category 2 DQFs are unconditional data cuts applied to any events generated by the algorithms. Category 3 DQFs define the clean data set used to calculate upper limits on the GW rates.

We define DQFs for S5y2/VSR1 following the approach used for S5y1 [12]. More details are given in Appendix A. After category 2 DQFs have been applied, the total available time during this period is 261.6 days for H1, 253.4 days for H2, 233.7 days for L1 and 106.2 days for V1 [19].

B. Candidate event generation

As discussed in Sec. IV, three independent search algorithms are used to identify possible GW bursts: exponential Gaussian correlator (EGC), Ω-pipeline (Ω), and coherent waveBurst (cWB). We analyze data from time intervals when at least two detectors were operating in coincidence. Altogether, eight networks, or sets of detectors, operating during mutually exclusive time periods are analyzed by at least one algorithm. Table I shows the time available for analysis (''live time'') for the different network configurations after application of category 1 and 2 DQFs. The actual times searched by each algorithm for each network (''observation times'') reflect details of the algorithms, such as the smallest analyzable data block, as well as choices about which networks are most suitable for each algorithm. The three- and two-detector network configurations not shown in Table I have negligible live time and are not considered in this search.

LIGO and GEO 600 data are sampled at 16 384 Hz, yielding a maximum bandwidth of 8192 Hz, while Virgo

TABLE I. Exclusive live time in days for each detector network configuration after category 2 DQFs (second column) and the observation time analyzed by each of the search algorithms (last three columns). The cWB algorithm did not process the L1V1 network because the coherent likelihood regulator used in this analysis was suboptimal for two detectors with very different orientations. Omega used a coherent combination of H1 and H2 as an effective detector and thus analyzed networks either with both or with neither. EGC analyzed only data with three or more interferometers during the part of the run when Virgo was operational.

network	live time	cWB	Ω	EGC
H1H2L1V1	68.9	68.2	68.7	66.6
H1H2L1	124.6	123.2	123.4	16.5
H1H2V1	15.8	15.7	15.1	15.3
H1L1V1	4.5	4.2	···	4.4
H1H2	35.4	35.2	34.8	···
H1L1	7.2	5.9	···	···
L1V1	6.4	···	6.3	···
H2L1	3.8	3.5	···	···

data are sampled at 20000 Hz. Because of the large calibration uncertainties at high frequency, only data below 6000 Hz are used in the search. Also, because of high seismic noise, the frequency band below 50 Hz is excluded from the analysis. Furthermore, the EGC search was limited to the 300–5000 Hz band over which Virgo's sensitivity was comparable to LIGO's. In Sec. VI we describe the influence of the calibration uncertainties on the results of the search.

C. Vetoes

After gravitational-wave candidate events are identified by the search algorithms, they are subject to additional ''veto'' conditions to exclude events occurring within certain time intervals. These vetoes are based on statistical correlations between transients in the GW channel (data stream) and the environmental and interferometric auxiliary channels.

We define vetoes for S5y2/VSR1 following the approach used for S5y1 [12]. More details are given in Appendix B.

D. Background estimation and tuning

To estimate the significance of candidate GW events, and to optimize event selection cuts, we need to measure the distribution of events due to background noise. With a multidetector analysis one can create a sample of background noise events and study its statistical properties. These samples are created by time-shifting data of one or more detectors with respect to the others by ''unphysical'' time delays (i.e. much larger than the maximum time-of-flight of a GW signal between the detectors). Shifts are typically in the range from $\sim$1 s to a few minutes. Any triggers that are coincident in the time-shifted data cannot be due to a true gravitational-wave signal; these coincidences therefore sample the noise background. Background estimation is done separately for each algorithm and network combination, using hundreds to thousands of shifts. To take into account possible correlated noise transients in the H1 and H2 detectors, which share a common environment and vacuum system, no time-shifts are introduced between these detectors for any network combination including another detector.

The shifted and unshifted data are analyzed identically. A portion of the background events are used together with simulations (see below) to tune the search thresholds and selection cuts; the remainder is used to estimate the significance of any candidate events in the unshifted data after the final application of the selection thresholds. All tuning is done purely on the time-shifted data and simulations prior to examining the unshifted data set. This ''blind'' tuning avoid any biases in our candidate selection. The final event thresholds are determined by optimizing the detection efficiency of the algorithms at a fixed false alarm rate.

E. Hardware and software injections

At pseudorandom times during the run, simulated burst signals were injected (added) into the interferometers by sending precalculated waveforms to the mirror position control system. These ''hardware injections'' provided an end-to-end verification of the detector instrumentation, the data acquisition system and the data analysis software. The injection times were clearly marked in the data with a DQF. Most of hardware injections were incoherent, i.e., performed into a single detector with no coincident injection into the other detectors. Some injections were performed coherently by taking into account a simulated source location in the sky and the angle-dependent sensitivity of the detectors to the two wave polarization states.

In addition to the flagged injections, a ''blind injection challenge'' was undertaken in which a small number (possibly zero) of coherent hardware injections were performed *without* being marked by a DQF. Information about these blind injections (including whether the number was nonzero) was hidden from the data analysis teams during the search, and revealed only afterward. This challenge was intended to test our data analysis procedures and decision processes for evaluating any candidate events that might be found by the search algorithms.

To determine the sensitivity of our search to gravitational waves, and to guide the tuning of selection cuts, we repeatedly reanalyze the data with simulated signals injected in software. The same injections are analyzed by all three analysis pipelines. See Sec. V for more details.

IV. SEARCH ALGORITHMS

Anticipated sources of gravitational wave bursts are usually not understood well enough to generate waveforms accurate and precise enough for matched filtering of generic signals. While some sources of GW bursts are being modeled with increasing success, the results tend to be highly dependent on physical parameters which may span a large parameter space. Indeed, some burst signals, such the white-noise burst from turbulent convection in a core-collapse supernova, are stochastic in nature and so are inherently not templatable. Therefore usually more robust excess-power algorithms [20–23] are employed in burst searches. By measuring power in the data as a function of time and frequency, one may identify regions where the power is not consistent with the anticipated fluctuations of detector noise. To distinguish environmental and instrumental transients from true GW signals, a multidetector analysis approach is normally used, in which the event must be seen in more than one detector to be considered a candidate GW.

The simplest multidetector analysis strategy is to require that the events identified in the individual detectors are coincident in time. The time coincidence window which should be chosen to take into account the possible time delays of a GW signal arriving at different sites, calibration

and algorithmic timing biases, and possible signal model dependencies. Time coincidence can be augmented by requiring also an overlap in frequency. One such time-frequency coincidence method used in this search is the EGC algorithm [24] (see also Appendix C). It estimates the signal-to-noise ratio (SNR) ρ_k in each detector k and uses the combined SNR $\rho_{\rm comb} = \sqrt{\sum_k \rho_k^2}$ to rank candidate events.

A modification of the time-frequency coincidence approach is used in the Ω search algorithm [25] (also see Appendix D). In Ω, the identification of the H1H2 network events is improved by coherently combining the H1 and H2 data to form a single pseudodetector data stream H_+. This algorithm takes an advantage of the fact that the colocated and coaligned H1 and H2 detectors have identical responses to a GW signal. The performance of the Ω algorithm is further enhanced by requiring that no significant power is left in the H1 $-$ H2 null stream, H_-, where GW signals cancel. This veto condition helps to reduce the false alarm rate due to random coincidences of noise transients, which typically leave significant power in the null stream. Network events identified by Ω are characterized by the strength $Z = \rho^2/2$ of the individual detector events, and by the correlated H1H2 energy $Z_{H_+}^{\rm corr}$.

A different network analysis approach is used in the cWB search algorithm [26] (see also [12] and Appendix E). The cWB algorithm performs a least-squares fit of a common GW signal to the data from the different detectors using the constrained likelihood method [27]. The results of the fit are estimates of the h_+ and $h_\times$ waveforms, the most probable source location in the sky, and various likelihood statistics used in the cWB selection cuts. One of these is the maximum likelihood ratio L_m, which is an estimator of the total SNR detected in the network. A part of the L_m statistic depending on pairwise combinations of the detectors is used to construct the network correlated amplitude η, which measures the degree of correlation between the detectors. Random coincidences of noise transients typically give low values of η, making this statistic useful for background rejection. The contribution of each detector to the total SNR is weighted depending on the variance of the noise and angular sensitivity of the detectors. The algorithm automatically marginalizes a detector with either elevated noise or unfavorable antenna patterns, so that it does not limit the sensitivity of the network.

V. SIMULATED SIGNALS AND EFFICIENCIES

The detection efficiencies of the search algorithms depend on the network configuration, the selection cuts used in the analysis, and the GW morphologies which may span a wide range of signal durations, frequencies and amplitudes. To evaluate the sensitivity of the search and verify that the search algorithms do not have a strong model dependency, we use several sets of ad-hoc waveforms. These include

(i) Sine-Gaussian waveforms:

$$h_+(t) = h_0 \sin(2\pi f_0 t) \exp[-(2\pi f_0 t)^2/2Q^2], \quad (5.1)$$

$$h_\times(t) = 0. \quad (5.2)$$

We use a discrete set of central frequencies f_0 from 70 Hz to 6000 Hz and quality factors Q of 3, 9, and 100; see Table II and Fig. 2 (top). The amplitude factor h_0 is varied to simulate GWs with different strain amplitudes. For definition of the polarizations, see Eq. (5.8) and text below it.

(ii) Gaussian waveforms:

$$h_+(t) = h_0 \exp(-t^2/\tau^2), \quad (5.3)$$

$$h_\times(t) = 0, \quad (5.4)$$

where the duration parameter τ is chosen to be one of (0.1, 1.0, 2.5, 4.0) ms; see Fig. 2 (middle).

(iii) Harmonic ringdown signals:

$$h_+(t) = h_{0,+} \cos(2\pi f_0 t) \exp[-t/\tau], \quad t > 1/(4f_0), \quad (5.5)$$

$$h_\times(t) = h_{0,\times} \sin(2\pi f_0 t) \exp[-t/\tau], \qquad t > 0. \quad (5.6)$$

We use several central frequencies f_0 from 1590 Hz to 3067 Hz, one long decay time, $\tau = 200$ ms, and two short decay times, 1 ms and 0.65 ms; see Table III and Fig. 2 (bottom). Two polarization states are used: circular ($h_{0,+} = h_{0,\times}$), and linear ($h_{0,+} = 0$). The quarter-cycle delay in h_+ is to avoid starting the waveform with a large jump.

(iv) Band-limited white noise signals:
These are bursts of Gaussian noise which are white over a frequency band $[f_{\rm low}, f_{\rm low} + \Delta f]$ and which have a Gaussian time profile with standard deviation decay time τ; see Table IV. These signals are unpolarized in the sense that the two polarizations h_+ and $h_\times$ have equal RMS amplitudes and are uncorrelated with each other. The strengths of the *ad hoc* waveform injections are characterized by the root-square-sum amplitude $h_{\rm rss}$,

$$h_{\rm rss} = \sqrt{\int_{-\infty}^{+\infty} dt(|h_+(t)|^2 + |h_\times(t)|^2)}. \quad (5.7)$$

The parameters of these waveforms are selected to coarsely cover the frequency range of the search from $\sim$50 Hz to $\sim$6 kHz, and duration of signals up to a few hundreds of milliseconds. The Gaussian, sine-Gaussian and ringdown waveforms explore the space of GW signals with small time-frequency volume, while the white noise

TABLE II. Values of $h_{\rm rss}^{50\%}$ and $h_{\rm rss}^{90\%}$ (for 50% and 90% detection efficiency), in units of 10^{-22} Hz$^{-1/2}$, for sine-Gaussian waveforms with the central frequency f_0 and quality factor Q. Three columns in the middle are the $h_{\rm rss}^{50\%}$ measured with the individual search algorithms for the H1H2L1V1 network. The next column is the $h_{\rm rss}^{50\%}$ of the logical OR of the cWB and Ω algorithms for the H1H2L1V1 network. The last two columns are the $h_{\rm rss}^{50\%}$ and the $h_{\rm rss}^{90\%}$ of the logical OR of the algorithms and networks (H1H2L1V1 or H1H2L1 or H1H2). All $h_{\rm rss}$ values take into account statistical and systematic uncertainties as explained in Sec. VI.

f_0	Q	H1H2L1V1, $h_{\rm rss}^{50\%}$				all networks	
[Hz]		cWB	Ω	EGC	cWB or Ω	$h_{\rm rss}^{50\%}$	$h_{\rm rss}^{90\%}$
70	3	17.9	26.7	···	17.6	20.4	96.6
70	9	20.6	34.4	···	20.6	25.0	120
70	100	20.5	35.0	···	20.0	25.1	121
100	9	9.2	14.1	···	9.1	10.6	49.7
153	9	6.0	9.1	···	6.0	6.5	29.3
235	3	6.5	6.6	···	5.9	6.1	28.8
235	9	6.4	5.8	···	5.6	5.6	26.8
235	100	6.5	6.7	···	6.2	6.0	26.1
361	9	10.5	10.2	60.1	9.5	10.0	42.0
554	9	11.1	10.5	18.8	9.9	10.9	47.1
849	3	19.2	15.8	30.0	15.3	15.8	73.8
849	9	17.7	15.3	28.5	14.6	15.8	71.5
849	100	16.0	16.2	31.3	14.5	15.3	66.7
1053	9	22.4	19.0	33.8	18.3	19.4	86.9
1304	9	28.1	23.6	41.0	22.6	24.7	115
1451	9	28.6	···	43.3	28.6	30.2	119
1615	3	39.6	32.1	48.4	31.7	33.8	146
1615	9	33.7	28.1	51.1	27.3	29.5	138
1615	100	29.6	30.6	53.8	27.6	28.6	126
1797	9	36.5	···	57.8	36.5	38.3	146
2000	3	42.6	···	···	42.6	47.1	191
2000	9	40.6	···	58.7	40.6	44.0	177
2000	100	34.9	···	···	34.9	38.4	153
2226	9	46.0	···	68.6	46.0	51.1	187
2477	3	61.9	···	···	61.9	65.6	262
2477	9	53.5	···	76.7	53.5	56.1	206
2477	100	44.5	···	···	44.5	48.9	201
2756	9	60.2	···	82.2	60.2	64.4	248
3067	3	86.9	···	···	86.9	87.0	343
3067	9	69.0	···	96.6	69.0	75.0	286
3067	100	55.4	···	···	55.4	61.1	273
3413	9	75.9	···	108	75.9	82.9	323
3799	9	89.0	···	116	89.0	97.7	386
4225	9	109	···	138	109	115	575
5000	3	207	···	···	207	187	1160
5000	9	126	···	155	126	130	612
5000	100	84.7	···	···	84.7	100	480
6000	9	182	···	···	182	196	893

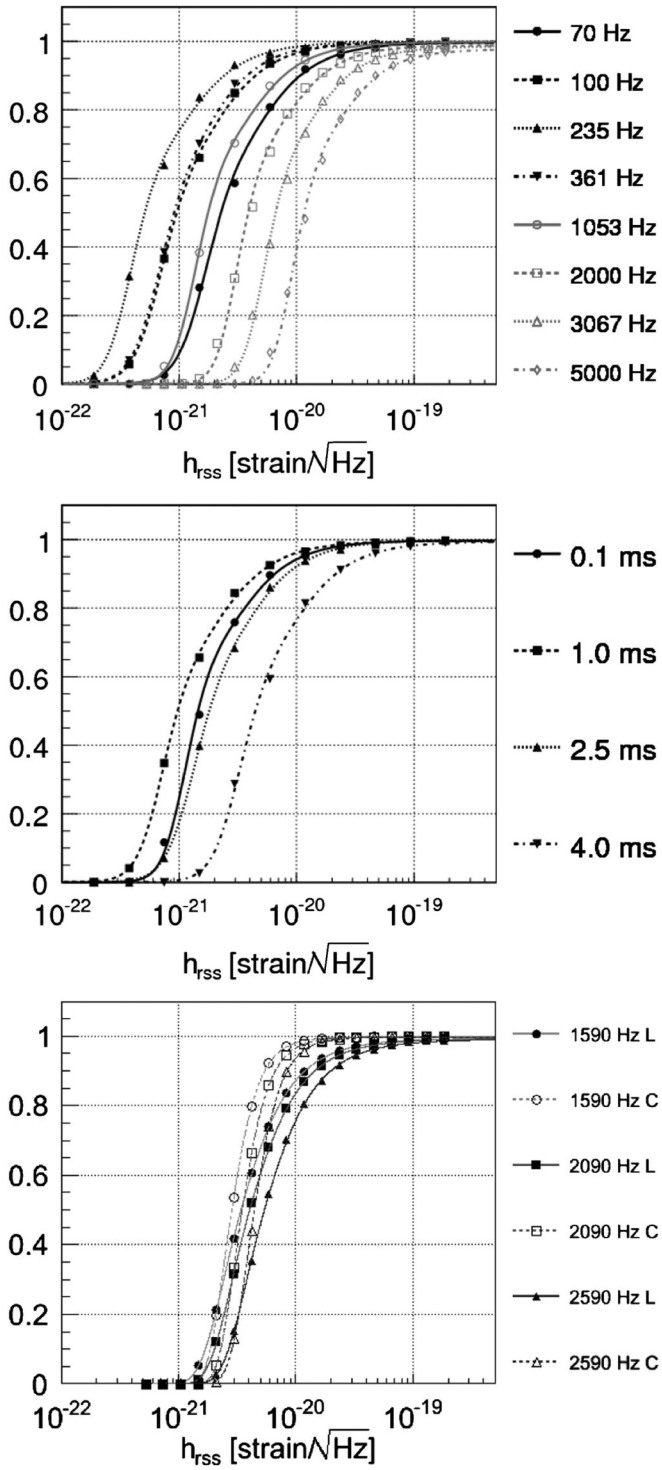

FIG. 2. Efficiency for selected waveforms as a function of signal amplitude $h_{\rm rss}$ for the logical OR of the H1H2L1V1, H1H2L1, and H1H2 networks. Top: sine-Gaussians with $Q = 9$ and central frequency spanning between 70 and 5000 Hz. Middle: Gaussians with τ between 0.1 and 4.0 ms. Bottom: linearly (L) and circularly (C) polarized ringdowns with $\tau = 200$ ms and frequencies between 1590 and 2590 Hz.

TABLE III. Values of $h_{\rm rss}^{50\%}$ and $h_{\rm rss}^{90\%}$ (for 50% and 90% detection efficiency using cWB), in units of 10^{-22} Hz$^{-1/2}$, for linearly and circularly polarized ringdowns characterized by parameters f and τ. All $h_{\rm rss}$ values take into account statistical and systematic uncertainties as explained in Sec. VI.

f	τ	all networks, $h_{\rm rss}^{50\%}$		all networks, $h_{\rm rss}^{90\%}$	
[Hz]	[ms]	Lin.	Circ.	Lin.	Circ.
1590	200	34.7	30.0	131	60.0
2000	1.0	49.5	43.8	155	81.1
2090	200	43.3	36.5	155	72.9
2590	200	58.6	46.0	229	88.8
3067	0.65	88.2	73.3	369	142

bursts explore the space of GW signals with relatively large time-frequency volume. Although the simulated waveforms are not physical, they may be similar to some waveforms produced by astrophysical sources. For example, the sine-Gaussian waveforms with few cycles are qualitatively similar to signals produced by the mergers of two black holes [2]. The long-timescale ringdowns are similar to signals predicted for excitation of neutron-star fundamental modes [28]. Some stellar collapse and core-collapse supernova models predict signals that resemble short ringdown waveforms (in the case of a rapidly rotating progenitor star) or band-limited white-noise waveforms with random polarizations. In the context of the recently proposed acoustic mechanism for core-collapse supernova explosions, quasiperiodic signals of $\gtrsim 500$ ms duration have been proposed [4].

TABLE IV. Values of $h_{\rm rss}^{50\%}$ and $h_{\rm rss}^{90\%}$ (for 50% and 90% detection efficiency), in units of 10^{-22} Hz$^{-1/2}$, for band-limited noise waveforms characterized by parameters $f_{\rm low}$, Δf, and τ. Two columns in the middle are the $h_{\rm rss}^{50\%}$ for the individual search algorithms for the H1H2L1V1 network. The next column is the $h_{\rm rss}^{50\%}$ of the logical OR of the cWB and Ω algorithms for the H1H2L1V1 network. The last two columns are the $h_{\rm rss}^{50\%}$ and the $h_{\rm rss}^{90\%}$ of the logical OR of the algorithms and networks (H1H2L1V1 or H1H2L1 or H1H2). All $h_{\rm rss}$ values take into account statistical and systematic uncertainties as explained in Sec. VI.

$f_{\rm low}$	Δf	τ	H1H2L1V1, $h_{\rm rss}^{50\%}$			all networks	
[Hz]	[Hz]	[ms]	cWB	Ω	cWB or Ω	$h_{\rm rss}^{50\%}$	$h_{\rm rss}^{90\%}$
100	100	0.1	7.6	13.6	7.6	8.4	19.6
250	100	0.1	9.1	10.2	8.8	8.6	18.7
1000	10	0.1	20.9	28.6	21.0	21.8	52.6
1000	1000	0.01	36.8	38.2	35.0	36.3	74.7
1000	1000	0.1	60.3	81.7	60.7	63.5	140
2000	100	0.1	40.4	···	40.4	44.1	94.4
2000	1000	0.01	60.7	···	60.7	62.4	128
3500	100	0.1	74.3	···	74.3	84.8	182
3500	1000	0.01	103	···	103	109	224
5000	100	0.1	101	···	101	115	255
5000	1000	0.01	152	···	152	144	342

To test the range for detection of gravitational waves from neutron-star collapse, two waveforms were taken from simulations by Baiotti *et al.* [5]. These waveforms, denoted D1 and D4, represent the extremes of the parameter space in mass and spin considered in that work. They are linearly polarized ($h_\times = 0$), with the waveform amplitude varying with the inclination angle ι (between the wave propagation vector and symmetry axis of the source) as $\sin^2\iota$.

The simulated detector responses $h_{\rm det}$ are constructed as

$$h_{\rm det} = F_+(\theta, \phi, \psi)h_+ + F_\times(\theta, \phi, \psi)h_\times. \tag{5.8}$$

Here F_+ and $F_\times$ are the detector antenna patterns, which depend on the direction to the source (θ, ϕ) and the polarization angle ψ. (The latter is defined as in Appendix B of [20].) These parameters are chosen randomly for each injection. The sky direction is isotropically distributed, and the polarization angle is uniformly distributed on $[0, \pi)$. For the ad-hoc waveforms no dependence on the inclination angle ι is simulated. The injections are distributed uniformly in time across the S5y2/VSR1 run, with an average separation of 100 s.

The detection efficiency after application of all selection cuts was determined for each waveform type. All waveforms were evaluated using cWB, while subsets were evaluated using Ω and EGC, due mainly to the limited frequency bands covered by those algorithms as they were used in this search (48–2048 Hz and 300–5000 Hz, respectively). Figure 2 shows the combined efficiency curves for selected sine-Gaussian, Gaussian and ringdown simulated signals as a function of the $h_{\rm rss}$ amplitude. Figure 3 shows the detection efficiency for the astrophysical signals D1 and D4 as a function of the distance to the source.

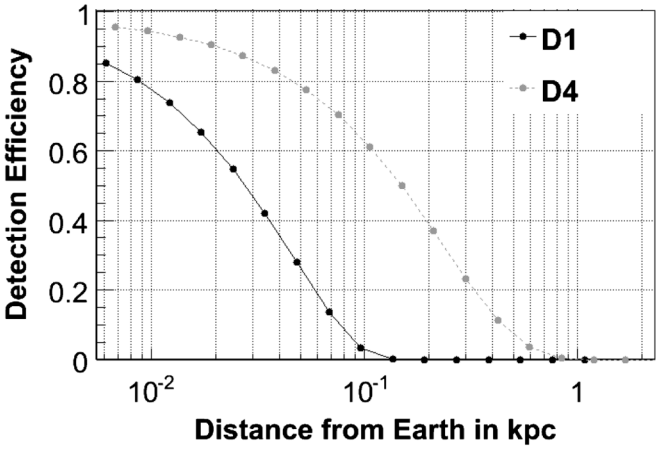

FIG. 3. Efficiency of the H1H2L1V1 network as a function of distance for the D1 and D4 waveforms of Baiotti *et al.* [5] predicted by polytropic general-relativistic models of neutron star collapse. These efficiencies assume random sky location, polarization and inclination angle.

Each efficiency curve is fitted with an empirical function and the injection amplitude for which that function equals 50% is determined. This quantity, $h_{\rm rss}^{50\%}$, is a convenient characterization of the sensitivity of the search to that waveform morphology. Tables II, III, and IV summarize the sensitivity of the search to the sine-Gaussian, ringdown, and band-limited white noise burst signals. Where possible, we also calculate the sensitivity of the logical OR of the cWB and Ω algorithms (since those two are used for the upper limit calculation as described in Sec. VII), and for the appropriately weighted combination of all networks (some of which are less sensitive) contributing to the total observation time. In general, the efficiency of the combination of the search algorithms is slightly more sensitive than the individual algorithms.

VI. UNCERTAINTIES

The amplitude sensitivities presented in this paper, i.e. the $h_{\rm rss}$ values at 50% and 90% efficiency, have been adjusted upward to conservatively reflect statistical and systematic uncertainties. The statistical uncertainty arises from the limited number of simulated signals used in the efficiency curve fit, and is typically a few percent. The dominant source of systematic uncertainty comes from the amplitude calibration: the single detector amplitude calibration uncertainties is typically of order 10%. Negligible effects are due to phase and timing uncertainties.

The amplitude calibration of the interferometers is less accurate at high frequencies than at low frequencies, and therefore two different approaches to handling calibration uncertainties are used in the S5y2/VSR1 search. In the frequency band below 2 kHz, we use the procedure established for S5y1 [13]. We combine the amplitude uncertainties from each interferometer into a single uncertainty by calculating a combined root-sum-square amplitude SNR and propagating the individual uncertainties assuming each error is independent: as a conservative result, the detection efficiencies are rigidly shifted towards higher $h_{\rm rss}$ by 11.1%. In the frequency band above 2 kHz, a new methodology, based on Monte Carlo simulations has been adopted to marginalize over calibration uncertainties: basically, we inject signals whose amplitude has been jittered according to the calibration uncertainties. The effect of miscalibration resulted in the increase of the combined $h_{\rm rss}^{50\%}$ by 3% to 14%, depending mainly on the central frequency of the injected signals.

VII. SEARCH RESULTS

In Sec. III we described the main steps in our search for gravitational-wave bursts. In the search all analysis cuts and thresholds are set in a blind way, using time-shifted (background) and simulation data. The blind cuts are set to yield a false-alarm rate of approximately 0.05 events or less over the observation time of each search algorithm, network configuration, and target frequency band. Here we describe the results.

A. Candidate events

After these cuts are fixed, the unshifted events are examined and the various analysis cuts, DQFs, and vetoes are applied. Any surviving events are considered as candidate gravitational-wave events and subject to further examination. The purpose of this additional step is to go beyond the binary decision of the initial cuts and evaluate additional information about the events which may reveal their origin. This ranges from ''sanity checks'' to deeper investigations on the background of the observatory, detector performances, environmental disturbances and candidate signal characteristics.

Examining the unshifted data, we found one foreground event among all the different search algorithms and detector combinations that survives the blind selection cuts. It was produced by cWB during a time when all five detectors were operating simultaneously. As the possible first detection of a gravitational-wave signal, this event was examined in great detail according to our follow-up checklist. We found no evident problem with the instruments or data, and no environmental or instrumental disturbance detected by the auxiliary channels. The event was detected at a frequency of 110 Hz, where all detectors are quite nonstationary, and where both the GEO 600 and Virgo detectors had poorer sensitivity (see Fig. 1). Therefore, while the event was found in the H1H2L1V1 analysis, we also reanalyzed the data using cWB and the H1H2L1 network. Figure 4 (top) shows the event above the blind selection cuts and the comparison with the measured H1H2L1 background of cWB in the frequency band below 200 Hz.

No foreground event passes the blind selection cuts in the Ω H1H2L1 analysis [see Fig. 4 (bottom)]; moreover, there is no visible excess of foreground events with respect to the expected background. The cWB event is well within the tail of the Ω foreground and does not pass the final cut placed on correlated energy of the Hanford detectors. Furthermore, the event is outside of the frequency band (300–5000 Hz) processed by the EGC algorithm. Figure 5 (top) shows the corresponding EGC foreground and background distributions for the H1H2L1V1 network. For comparison, Fig. 5 (bottom) shows similar distributions from cWB, with no indication of any excess of events in the frequency band 1200–6000 Hz.

To better estimate the significance of the surviving cWB event, we performed extensive background studies with cWB for the H1H2L1 network, accumulating a background sample with effective observation time of approximately 500 years. These studies indicate an expected false alarm rate for similar events of once per 43 years for the cWB algorithm and the H1H2L1 network. The statistical significance of the event must take into account a ''trials factor'' arising from multiple analyses using different

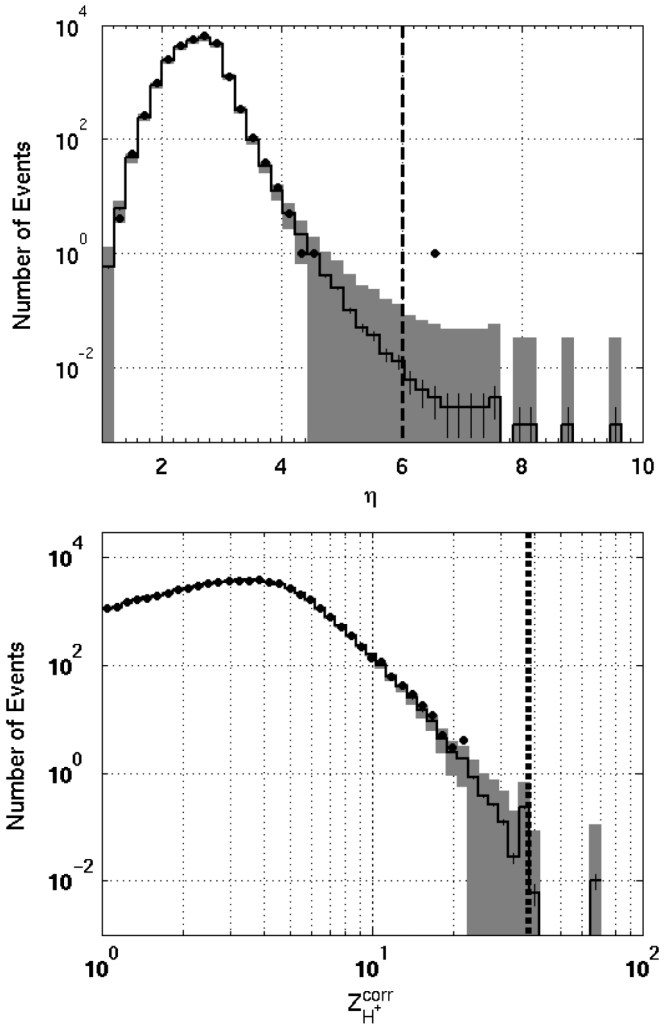

FIG. 4. Distribution of background (solid line) and foreground (solid dots) events from the search below 200 Hz in the H1H2L1 network, after application of category 2 data quality and vetoes: cWB (top), Ω (bottom). The event-strength figures of merit on the horizontal axes are defined in the appendices on the search algorithms. The small error bars on the solid line are the 1σ statistical uncertainty on the estimated background, while the wider gray belt represents the expected root-mean-square statistical fluctuations on the number of background events in the foreground sample. The loudest foreground event on the top plot is the only event that survived the blind detection cuts of this search, shown as vertical dashed lines. This event was later revealed to have been a blind injection.

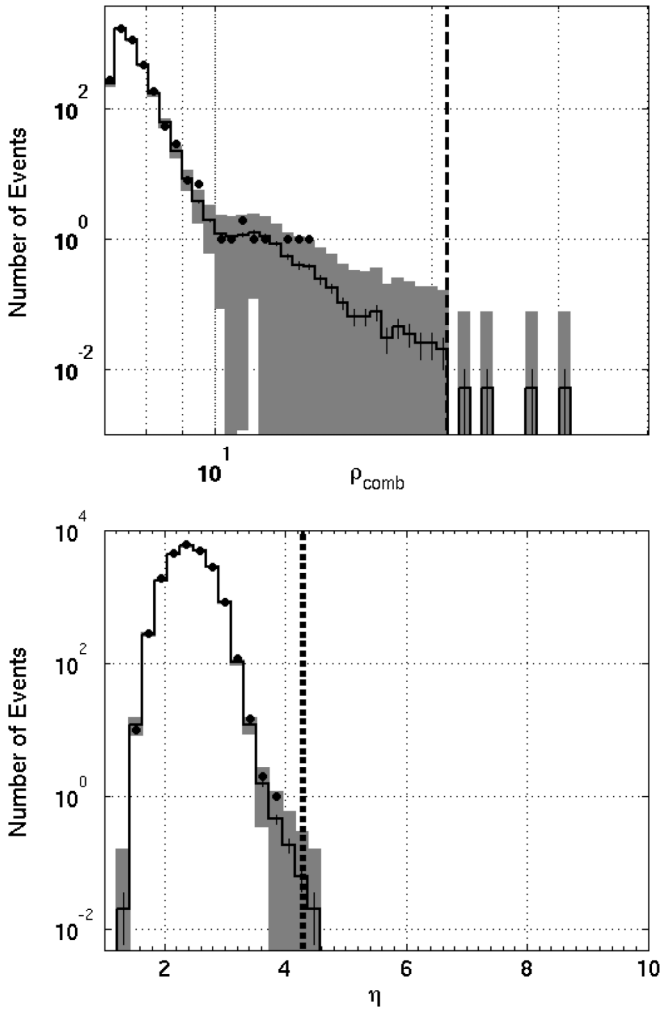

FIG. 5. Distribution of background (solid line) and foreground (solid dots) H1H2L1V1 events after category 2 data quality and vetoes: EGC events in the frequency band 300–5000 Hz (top), cWB events in the frequency band 1200–6000 Hz (bottom). The event-strength figures of merit on the horizontal axes are defined in the appendices on the search algorithms. The small error bars on the solid line are the 1σ statistical uncertainty on the estimated background, while the wider gray belt represents the expected root-mean-square statistical fluctuations on the number of background events in the foreground sample.

search algorithms, networks and frequency bands. Neglecting a small correlation among the backgrounds, this factor can be estimated by considering the total effective analyzed time of all the independent searches, which is 5.1 yr. The probability of observing one event at a background rate of once per 43 years or less in any of our searches is then on the order of 10%. This probability was considered too high to exclude a possible accidental origin of this event, which was neither confirmed nor ruled out as a plausible GW signal. This event was later revealed to be a hardware injection with $h_{\rm rss} = 1.0 \times 10^{-21}$ Hz$^{-1/2}$. It was the only burst injection within the "blind injection challenge." Therefore it was removed from the analysis by the cleared injection data quality flag. We can report that cWB recovered the injection parameters and waveforms faithfully, and the exercise of treating the event as a real GW candidate was a valuable learning experience.

Although no other outstanding foreground events were observed in the search, we have additionally examined events in the data set with relaxed selection cuts, namely, before applying category 3 DQFs and vetoes. In this set we find a total of three foreground events. One of these is produced by the EGC algorithm (0.16 expected from the

background) and the other two are from the Ω-pipeline (1.4 expected). While an exceptionally strong event in the enlarged data set could, in principle, be judged to be a plausible GW signal, none of these additional events is particularly compelling. The EGC event occurred during a time of high seismic noise and while the H2 interferometer was reacquiring lock (and thus could occasionally scatter light into the H1 detector), both of which had been flagged as category 3 data quality conditions. The Ω-pipeline events fail the category 3 vetoes due to having corresponding glitches in H1 auxiliary channels. None of these three events passes the cWB selection cuts. For these reasons, we do not consider any of them to be a plausible gravitational-wave candidate. Also, since these events do not pass the predefined category 3 data quality and vetoes, they do not affect the calculation of the upper limits presented below.

B. Upper limits

The S5y2/VSR1 search includes the analysis of eight network configurations with three different algorithms. We use the method presented in [29] to combine the results of this search, together with the S5y1 search [12], to set frequentist upper limits on the rate of burst events. Of the S5y2 results, we include only the networks H1H2L1V1, H1H2L1 and H1H2, as the other networks have small observation times and their contribution to the upper limit would be marginal. Also, we decided *a priori* to use only the two algorithms which processed the data from the full S5y2 run, namely, cWB and Ω. (EGC only analyzed data during the ~5 months of the run when Virgo was operational.) We are left therefore with six analysis results to combine with the S5y1 results to produce a single upper limit on the rate of GW bursts for each of the signal morphologies tested.

As discussed in [29], the upper limit procedure combines the sets of surviving triggers according to which algorithm(s) and/or network detected any given trigger, and weights each trigger according to the detection efficiency of that algorithm and network combination. For the special case of no surviving events, the 90% confidence upper limit on the total event rate (assuming a Poisson distribution of astrophysical events) reduces to

$$R_{90\%} = \frac{2.3}{\epsilon_{\rm tot} T}, \tag{7.1}$$

where $2.3 = -\log(1 - 0.9)$, $\epsilon_{\rm tot}$ is the detection efficiency of the union of all search algorithms and networks, and T is the total observation time of the analyzed data sets.

In the limit of strong signals in the frequency band below 2 kHz, the product $\epsilon_{\rm tot} T$ is 224.0 days for S5y1 and 205.3 days for S5y2/VSR1. The combined rate limit for strong GW signals is thus 2.0 $\rm yr^{-1}$. For the search above 2 kHz, the rate limit for strong GW signals is 2.2 $\rm yr^{-1}$. This slightly weaker limit is due to the fact that less data was analyzed in the S5y1 high-frequency search than in the

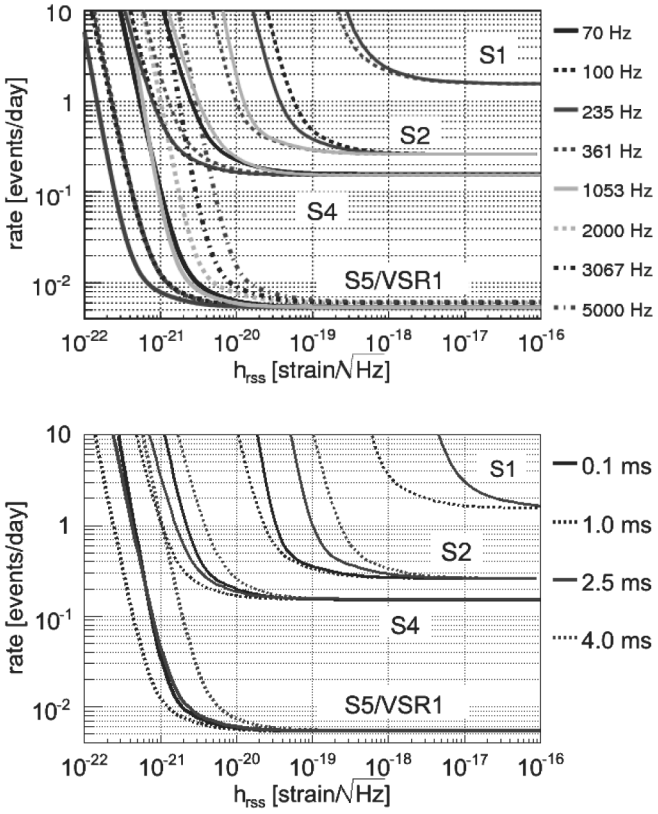

FIG. 6. Selected exclusion diagrams showing the 90% confidence rate limit as a function of signal amplitude for $Q = 9$ sine-Gaussian (top) and Gaussian (bottom) waveforms for the results of the entire S5 and VSR1 runs (S5/VSR1) compared to the results reported previously (S1, S2, and S4).

S5y1 low-frequency search (only 161.3 days of H1H2L1 data [13]). Figure 6 shows the combined rate limit as a function of amplitude for selected Gaussian and sine-Gaussian waveforms.

The results can also be interpreted as limits on the rate density (number per time per volume) of GWBs assuming a standard-candle source. For example, given an isotropic distribution of sources with amplitude $h_{\rm rss}$ at a fiducial distance r_0, and with rate density $\mathcal{R}$, the rate of GWBs at the Earth with amplitudes in the interval $[h, h + dh]$ is

$$dN = \frac{4\pi \mathcal{R} (h_{\rm rss} r_0)^3}{h^4} dh. \tag{7.2}$$

(Here we have neglected the inclination angle ι; equivalently we can take h^2 to be averaged over $\cos\iota$.) The expected number of detections given the network efficiency $\epsilon(h)$ (for injections without any ι dependence) and the observation time T is

$$\begin{aligned} N_{\rm det} &= T \int_0^\infty dh \left(\frac{dN}{dh}\right) \epsilon(h) \\ &= 4\pi \mathcal{R} T (h_{\rm rss} r_0)^3 \int_0^\infty dh h^{-4} \epsilon(h). \end{aligned} \tag{7.3}$$

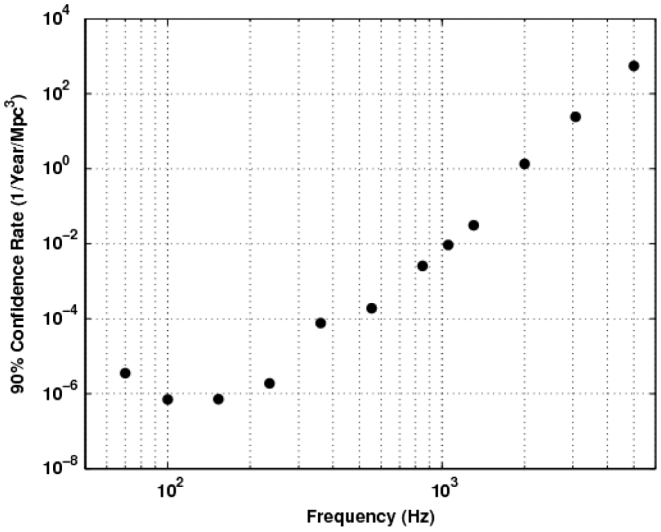

FIG. 7. Rate limit per unit volume at the 90% confidence level for a linearly polarized sine-Gaussian standard-candle with $E_{\rm GW} = M_\odot c^2$.

For linearly polarized signals distributed uniformly in $\cos\iota$, the efficiency is the same with h rescaled by a factor $\sin^2\iota$ divided by that factor's appropriately averaged value $\sqrt{8/15}$. Thus the above expression is multiplied by $\int_0^1 d\cos\iota (15/8)^{3/2}\sin^6\iota \approx 1.17$. The lack of detection candidates in the S5/VSR1 data set implies a 90% confidence upper limit on rate density $\mathcal{R}$ of

$$\mathcal{R}_{90\%} = \frac{2.0}{4\pi T (h_{\rm rss} r_0)^3 \int_0^\infty dh h^{-4} \epsilon(h)}. \qquad (7.4)$$

Assuming that a standard-candle source emits waves with energy $E_{\rm GW} = M_\odot c^2$, where $M_\odot$ is the solar mass, the product $h_{\rm rss} r_0$ is

$$h_{\rm rss} r_0 = \sqrt{\frac{G M_\odot}{c}} (\pi f_0)^{-1}. \qquad (7.5)$$

Figure 7 shows the rate density upper limits as a function of frequency. This result can be interpreted in the following way: given a source with a characteristic frequency f and energy $E_{\rm GW} = Mc^2$, the corresponding rate limit is $\mathcal{R}_{90\%}(f)(M_\odot/M)^{3/2}$ yr^{-1} Mpc^{-3}. For example, for sources emitting at 150 Hz with $E_{\rm GW} = 0.01 M_\odot c^2$, the rate limit is approximately 6×10^{-4} yr^{-1} Mpc^{-3}.

The bump at 361 Hz reflects the effect of the ''violin modes'' (resonant frequencies of the wires suspending the mirrors) on the sensitivity of the detector.

VIII. SUMMARY AND DISCUSSION

In this paper we present results of new all-sky untriggered searches for gravitational wave bursts in data from the first Virgo science run (VSR1 in 2007) and the second year of the fifth LIGO science run (S5y2 in 2006–2007). This data set represented the first long-term operation of a worldwide network of interferometers of similar performance at three different sites. Data quality and analysis algorithms are significantly improved since similar searches of the previous LIGO run (S4 in 2004) [30] and even since the first year of S5 (S5y1 in 2005–2006) [12,13]. This is reflected in an improved strain sensitivity with $h_{\rm rss}^{50\%}$ as low (good) as 5.6×10^{-22} Hz$^{-1/2}$ for certain waveforms (see Table II), compared to best values of 1.3×10^{-21} Hz$^{-1/2}$ and 6.0×10^{-22} Hz$^{-1/2}$ for S4 and S5y1, respectively. The new searches also cover an extended frequency band of 50–6000 Hz.

No plausible gravitational wave candidates have been identified in the S5y2/VSR1 searches. Combined with the S5y1 results, which had comparable observation time, this yields an improved upper limit on the rate of bursts (with amplitudes a few times larger than $h_{\rm rss}^{50\%}$) of 2.0 events per year at 90% confidence for the 64–2048 Hz band, and 2.2 events per year for higher-frequency bursts up to 6 kHz. Thus the full S5/VSR1 upper limit is better than the S5y1 upper limits of 3.75 per year (64–2000 Hz) and 5.4 per year (1–6 kHz), and is more than an order of magnitude better than the upper limit from S4 of 55 events per year.

We note that the IGEC network of resonant bar detectors set a slightly more stringent rate limit, 1.5 events per year at 95% confidence level [14]. However, those detectors were sensitive only around their resonant frequencies, near 900 Hz, and achieved that rate limit only for signal amplitudes (in $h_{\rm rss}$ units) of a few times 10^{-19} Hz$^{-1/2}$ or greater, depending on the signal waveform. (See Sec. X of [31] for a discussion of this comparison.) Further IGEC observations during 6 months of 2005 [15] improved the rate limit to $\simeq 8.4$ per year for bursts as weak as a few times 10^{-20} Hz$^{-1/2}$ but did not change the more stringent rate limit for stronger bursts. The current LIGO-Virgo burst search is sensitive to bursts with $h_{\rm rss}$ one to 2 orders of magnitude weaker than those which were accessible to the IGEC detectors.

To characterize the astrophysical sensitivity achieved by the S5y2/VSR1 search, we calculate the amount of mass, converted into GW burst energy at a given distance r_0, that would be sufficient to be detected by the search with 50% efficiency ($M_{\rm GW}$). Inverting Eq. (7.5), we obtain a rough estimate assuming an average source inclination angle (i.e. $h_{\rm rss}^2$ is averaged over $\cos\iota$):

$$M_{\rm GW} = \frac{\pi^2 c}{G} r_0^2 f_0^2 h_{\rm rss}^2. \qquad (8.1)$$

For example, consider a sine-Gaussian signal with $f_0 = 153$ Hz and $Q = 9$, which (from Table II) has $h_{\rm rss}^{50\%} = 6.0 \times 10^{-22}$ Hz$^{-1/2}$ for the four-detector network. Assuming a typical Galactic distance of 10 kpc, that $h_{\rm rss}$ corresponds to $M_{\rm GW} = 1.8 \times 10^{-8} M_\odot$. For a source in the

Virgo galaxy cluster, approximately 16 Mpc away, the same $h_{\rm rss}^{50\%}$ would be produced by a mass conversion of roughly $0.046 M_\odot$. These figures are slightly better than for the S5y1 search and a factor of ~5 better than the S4 search.

We also estimate in a similar manner a detection range for GW signals from core-collapse supernovae and from neutron star collapse to a black hole. Such signals are expected to be produced at a much higher frequency (up to a few kHz) and also with a relatively small GW energy output (10^{-9}–$10^{-5} M_\odot c^2$). For a possible supernova scenario, we consider a numerical simulation of core collapse by Ott *et al.* [32]. For the model s25WW, which undergoes an acoustically driven explosion, as much as $8 \times 10^{-5} M_\odot$ may be converted to gravitational waves. The frequency content produced by this particular model peaks around ~940 Hz and the duration is of order 1 s. Taking this to be similar to a high-Q sine-Gaussian or a long-duration white noise burst, from our detection efficiency studies we estimate $h_{\rm rss}^{50\%}$ of 17–22×10^{-22} Hz$^{-1/2}$, i.e. that such a signal could be detected out to a distance of around 30 kpc. The axisymmetric neutron star collapse signals D1 and D4 of Baiotti *et al.* [5] have detection ranges (at 50% confidence) of only about 25 pc and 150 pc (see Fig. 3, due mainly to their lower energy ($M_{\rm GW} < 10^{-8} M_\odot$) and also to emitting most of that energy at 2–6 kHz, where the detector noise is greater.

The Advanced LIGO and Virgo detectors, currently under construction, will increase the detection range of the searches by an order of magnitude, therefore increasing by ~1000 the monitored volume of the universe. With that sensitivity, GW signals from binary mergers are expected to be detected regularly, and other plausible sources may also be explored. Searches for GW burst signals, capable of detecting unknown signal waveforms as well as known ones, will continue to play a central role as we increase our understanding of the universe using gravitational waves.

ACKNOWLEDGMENTS

The authors gratefully acknowledge the support of the United States National Science Foundation for the construction and operation of the LIGO Laboratory, the Science and Technology Facilities Council of the United Kingdom, the Max-Planck-Society and the State of Niedersachsen/Germany for support of the construction and operation of the GEO 600 detector, and the Italian Istituto Nazionale di Fisica Nucleare and the French Centre National de la Recherche Scientifique for the construction and operation of the Virgo detector. The authors also gratefully acknowledge the support of the research by these agencies and by the Australian Research Council, the Council of Scientific and Industrial Research of India, the Istituto Nazionale di Fisica Nucleare of Italy, the Spanish Ministerio de Educación y Ciencia, the Conselleria d'Economia Hisenda i Innovació of the Govern de les Illes Balears, the Foundation for Fundamental Research on Matter supported by the Netherlands Organisation for Scientific Research, the Polish Ministry of Science and Higher Education, the FOCUS Programme of Foundation for Polish Science, the Royal Society, the Scottish Funding Council, the Scottish Universities Physics Alliance, the National Aeronautics and Space Administration, the Carnegie Trust, the Leverhulme Trust, the David and Lucile Packard Foundation, the Research Corporation, and the Alfred P. Sloan Foundation. This document has been assigned LIGO Laboratory document number LIGO-P0900108-v6.

APPENDIX A: DATA QUALITY FLAGS

The removal of poor-quality LIGO data uses the data quality flag (DQF) strategy described in the first year analysis [12]. For the second year there are several new DQFs. New category 2 flags mark high currents in the end test-mass side coils, discontinuous output from a tidal compensation feed-forward system, periods when an optical table was insufficiently isolated from ground noise, and power fluctuations in lasers used to thermally control the radius of curvature of the input test masses. A flag for overflows of several of the main photodiode readout sensors that was used as a category 3 flag in the first year was promoted to category 2. New category 3 flags mark noise transients from light scattered from H1 into H2 and vice versa, large low-frequency seismic motions, the optical table isolation problem noted above, periods when the roll mode of an interferometer optic was excited, problems with an optical level used for mirror alignment control, and one period when H2 was operating with degraded sensitivity. The total "dead time" (fraction of live time removed) during the second year of S5 due to category 1 DQFs was 2.4%, 1.4%, and <0.1% for H1, H2, and L1, respectively. Category 2 DQF dead time was 0.1%, 0.1%, and 0.6%, and category 3 DQF dead time was 4.5%, 5.5%, and 7.7%. Category 4 flags, used only as additional information for follow-ups of candidate events (if any), typically flag one-time events identified by Collaboration members on duty in the observatory control rooms, and thus are quite different between the first and second years.

Virgo DQFs are defined by study of the general behavior of the detector, daily reports from the control room, online calibration information, and the study of loud transient events generated online from the uncalibrated Virgo GW channel by the Qonline [33] program. Virgo DQFs include out-of-science mode, hardware injection periods, and saturation of the current flowing in the coil drivers. Most of them concern a well identified detector or data acquisition problem, such as the laser frequency stabilization process being off, photodiode saturation, calibration line dropouts,

and loss of synchronization of the longitudinal and angular control. Some loud glitches and periods of higher glitch rate are found to be due to environmental conditions, such as increased seismic noise (wind, sea, and earthquakes), and 50 Hz power line ground glitches seen simultaneously in many magnetic probes. In addition, a faulty piezoelectric driver used by the beam monitoring system generated glitches between 100 and 300 Hz, and a piezo controlling a mirror on a suspended bench whose cabling was not well matched caused glitches between 100 and 300 Hz and between 600 and 700 Hz. The total dead time in VSR1 due to category 1 DQFs was 1.4%. Category 2 DQF dead time was 2.6%, and category 3 DQF dead time was 2.5% [34].

APPENDIX B: EVENT-BY-EVENT VETOES

Event-by-event vetoes discard gravitational-wave channel noise events using information from the many environmental and interferometric auxiliary channels which measure non-GW degrees of freedom. Our procedure for identifying vetoes in S5y2 and VSR1 follows that used in S5y1 [12]. Both the GW channels and a large number of auxiliary channels are processed by the KleineWelle (KW) [35] algorithm, which looks for excess power transients. Events from the auxiliary channels which have a significant statistical correlation with the events in the corresponding GW channel are used to generate the veto time intervals. Candidate events identified by the search algorithms are rejected if they fall inside the veto time intervals.

Veto conditions belong to one of two categories which follow the same notation used for data quality flags. Category 2 vetoes are a conservative set of vetoes targeting known electromagnetic and seismic disturbances at the LIGO and Virgo sites. These are identified by requiring a coincident observation of an environmental disturbance across several channels at a particular site. The resulting category 2 data selection cuts are applied to all analyses described in this paper, and remove $\sim$0.2% of analyzable coincident live time. Category 3 vetoes make use of all available auxiliary channels shown not to respond to gravitational waves. An iterative tuning method is used to maximize the number of vetoed noise events in the gravitational-wave channel while removing a minimal amount of time from the analysis. The final veto list is applied to all analyses below 2048 Hz, removing $\sim$2% of total analyzable coincident live time.

An additional category 3 veto condition is applied to Virgo triggers, based on the ratio of the amplitude of an event as measured in the in-phase (P) and quadrature (Q) dark port demodulated signals. Since the Q channel should be insensitive to a GW signal, large Q/P ratio events are vetoed. This veto has been verified to be safe using hardware signal injections [36], with a loss of live time of only 0.036%.

APPENDIX C: EGC BURST SEARCH

The exponential Gaussian correlator (EGC) pipeline is based on a matched filter using exponential Gaussian templates [37,38],

$$\Phi(t) = \exp\left(-\frac{t^2}{2\tau_0^2}\right)e^{2\pi i f_0 t}, \tag{C1}$$

where f_0 is the central frequency and τ_0 is the duration. Assuming that real GWBs are similar to sine-Gaussians, EGC cross-correlates the data with the templates,

$$C(t) = \frac{1}{N}\int_{-\infty}^{+\infty}\frac{\tilde{x}(f)\tilde{\Phi}^*(f)}{S(f)}e^{2\pi i f t}df. \tag{C2}$$

Here $\tilde{x}(f)$ and $\tilde{\Phi}(f)$ are the Fourier transforms of the data and template, and $S(f)$ is the two-sided noise power spectral density. N is a template normalization factor, defined as

$$N = \sqrt{\int_{-\infty}^{+\infty}\frac{|\Phi(f)|^2}{S(f)}df}. \tag{C3}$$

We tile the parameter space (f_0, $Q_0 \equiv 2\pi\tau_0 f_0$) using the algorithm of [39]. The minimal match is 72%, while the average match between templates is 96%. The analysis covers frequencies from 300 Hz to 5 kHz, where LIGO and Virgo have comparable sensitivity. Q_0 varies from 2 to 100, covering a large range of GW burst durations.

The quantity $\rho = \sqrt{2|C|^2}$ is the signal-to-noise ratio (SNR), which we use to characterize the strength of triggers in the individual detectors. The analysis is performed on times when at least three of the four detectors were operating. Triggers are generated for each of the four detectors and kept if the SNR is above 5. In order to reduce the background, category 2 DQFs and vetoes are applied, followed by several other tests. First, triggers must be coincident in both time and frequency between a pair of detectors. The time coincidence window is the light travel time between the interferometers plus a conservative 10 ms allowance for the EGC timing accuracy. The frequency coincidence window is selected to be 350 Hz. Second, events seen in coincidence in H1 and H2 with a unexpected ratio in SNR are discarded (the SNR in H1 should be approximately 2 times that in H2). Surviving coincident triggers are ranked according to the combined SNR, defined as

$$\rho_{\mathrm{comb}} = \sqrt{\rho_1^2 + \rho_2^2}, \tag{C4}$$

where ρ_1 and ρ_2 are the SNR in the two detectors. Third, a threshold is applied on ρ_1 and ρ_2 to reduce the trigger rate in the noisier detector. This lowers the probability that a detector with a large number of triggers will generate many coincidences with a few loud glitches in the other detector. Finally, for each coincident trigger we compute the SNR disbalance measure

TABLE V. Thresholds and background tuning information for all the networks studied by the EGC pipeline.

Network	Obs. time [days]	# lags	FAR	ρ_{comb}
H1H2L1V1	66.6	200	<400 Hz: 1 event in 10 years	69.8
			>400 Hz: 0.05 events	21.0
H1H2L1	18.3	1000	<400 Hz: 1 event in 10 years	80.9
			>400 Hz: 0.05 events	10.0
H1H2V1	15.9	1000	<400 Hz: 1 event in 10 years	89.6
			>400 Hz: 0.05 events	15.4
H1L1V1	4.5	2000	<400 Hz: 1 event in 10 years	67.9
			>400 Hz: 0.01 events	24.2

$$\Lambda = \frac{\rho_{\mathrm{comb}}}{\rho_{\mathrm{comb}} + |\rho_1 - \rho_2|}. \tag{C5}$$

This variable is useful in rejecting glitches in a pair of coaligned detectors with similar sensitivity, and so is used primarily for pairs of triggers from the LIGO detectors.

The background is estimated for each detector pair by time shifting the trigger lists. 200 time slides are done for H1H2L1V1, and more for the three-detector networks due to their shorter observation times (see Table V). The thresholds applied to ρ_1, ρ_2 and Λ are tuned for each detector pair to maximize the average detection efficiency for sine-Gaussian waveforms at a given false alarm rate. Once the ρ_1, ρ_2 and Λ thresholds are applied, all trigger pairs from the network are considered together and ρ_{comb} is used as the final statistic to rank the triggers. A threshold is placed on ρ_{comb}, chosen to give a low false alarm rate. More precisely, as we observe an excess of loud glitches with $f_0 < 400$ Hz, we use different thresholds depending on the frequency of the coincident triggers. Below 400 Hz, the false alarm rate is tuned to 1 event per 10 years. Above, the threshold for each network is set to give a maximum of 0.05 events expected from background for that network. An exception is made for H1L1V1, where the maximum number is chosen to be 0.01 events because of its shorter observation time. The final thresholds for each network are given in Table V.

APPENDIX D: Ω-PIPELINE BURST SEARCH

The Ω-Pipeline is essentially identical to QPipeline, which was used in previous LIGO S5 searches [12,13]. QPipeline has since been integrated into a larger software suite, with a change in nomenclature but no significant change in methodology. Since this approach is discussed in detail in [12,21], we provide only a summary here.

The Ω-Pipeline, like EGC, functions as a matched-filter search on a single-interferometer basis. The data stream is whitened by linear predictive filtering [40], then projected onto a template bank of complex exponentials. These templates are similar to those used by EGC, parametrized by central time τ_0, central frequency f_0, and quality factor Q_0, but use bisquare windows rather than Gaussian windows. The template spacing is also different, selected for computational speed, rather than for strict mathematical optimization as in EGC. The Ω template bank has a minimal match of 80%, and covers a frequency range from 48 Hz to 2048 Hz and a Q range from 2.35 to 100.

The significance of a single-interferometer trigger is given by its normalized energy Z, defined as the ratio of the squared magnitude of X (the projection onto the best-matched template) for that trigger to the mean-squared magnitude of other templates with the same f_0 and Q_0. For Gaussian white noise, Z is exponentially distributed and related to the matched filter SNR ρ by

$$Z = |X|^2/\langle |X|^2 \rangle = \rho^2/2. \tag{D1}$$

Z is used to rank L1 and V1 triggers.

For H1 and H2, Ω-Pipeline takes advantage of their colocated nature to form two linear combinations of the data streams. The first of these, the *coherent* stream H_+, is the sum of the strains in the two interferometers weighted by their noise power spectral densities. We define the coherent energy Z_{H_+} following (D1). We also define the correlated energy $Z^{\mathrm{corr}}_{\mathrm{H}_+}$, which is obtained by removing the contribution to Z_{H_+} from H1 and H2 individually and leaving only the cross-correlation term [41]. The H1H2 cuts are based on $Z^{\mathrm{corr}}_{\mathrm{H}_+}$, because it is less susceptible than Z_{H_+} to instrumental glitches, so providing better separation between signal and noise. The second stream, the *null* stream H_-, is the difference between the strains in H1 and H2. The normalized energy Z_{H_-} should be small for a gravitational wave, but generally much larger for an instrumental glitch. We therefore veto coherent stream triggers which are coincident in time and frequency with null stream triggers.

We require triggers to be coincident in at least two detectors. The interferometer combinations analyzed are shown in Table VI. (Note that because of the coherent analysis of H1 and H2, both must be operating for data from either to be analyzed.) Triggers are required to be coincident in both time and frequency as follows:

$$|T_1 - T_2| < T_c + \tfrac{1}{2}\max(\sigma_1, \sigma_2) \tag{D2}$$

TABLE VI. Thresholds on normalized energy for the various detector combinations.

Detector combination and frequency band	threshold	events in 1000 timeslides
H1H2L1 <200 Hz	$Z_{H_+}^{\rm corr} > 37$, $Z_{L1} > 13$	14
H1H2L1 >200 Hz	$Z_{H_+}^{\rm corr} > 13$, $Z_{L1} > 13$	16
H1H2V1 <200 Hz	$Z_{H_+}^{\rm corr} > 22$, $Z_{V1} > 13$	9
H1H2V1 >200 Hz	$Z_{H_+}^{\rm corr} > 14$, $Z_{V1} > 13$	0
L1V1 <200 Hz	$Z_{L1} > 32$ and $Z_{V1} > (4.7 \times 10^{-13} Z_{L1})^{-0.3}$	4
L1V1 >200 Hz	$Z_{L1} > 30$ and $Z_{V1} > (6.9 \times 10^{-12} Z_{L1})^{-0.27}$	5
H1H2 <200 Hz	$Z_{H_+}^{\rm corr} > 80$	0 (10 slides)
H1H2 >200 Hz	$Z_{H_+}^{\rm corr} > 30$	0 (10 slides)
total events		48

$$|F_1 - F_2| < \tfrac{1}{2}\max(b_1, b_2). \quad \text{(D3)}$$

Here T and F are the central time and frequency of the triggers, σ and b are their duration and bandwidth, and T_c is the light travel time between the interferometers.

The background for each detector pair is determined by time-shifting the triggers from one detector. We use 1000 shifts for each pair, except H1-H2. Only 10 shifts between H1 and H2 are used because the coherent analysis requires each shift to be processed independently, substantially increasing the computational cost. Also, time shifts between H1 and H2 are less reliable because they miss correlated background noise from the common environment. For all pairs, triggers below and above 200 Hz are treated separately because of the different characteristics of the glitch populations at these frequencies.

Normalized energy thresholds are set separately for each detector combination and frequency range such that there is less than a 5% probability of a false alarm after category 3 DQFs and vetoes. Table VI shows the thresholds and surviving events in timeslides for each combination. Figure 8 shows background and injection triggers and the energy thresholds for one interferometer pair.

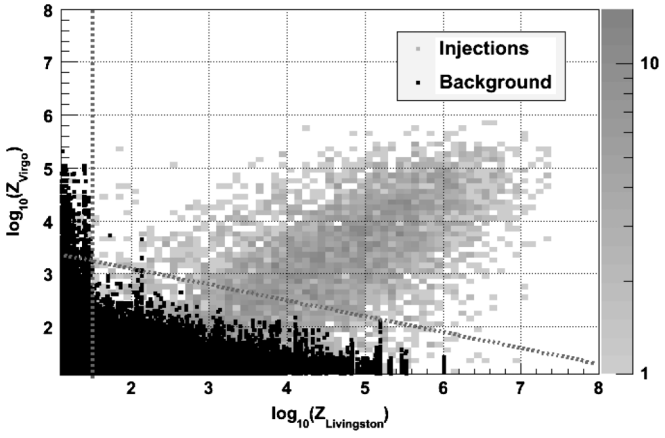

FIG. 8. Distribution of background and injection triggers below 200 Hz after category 3 DQFs and vetoes for L1-V1 pair. The dashed lines show the final normalized energy thresholds.

APPENDIX E: COHERENT WAVEBURST SEARCH

Coherent waveBurst (cWB) is a coherent algorithm for detecting gravitational-wave bursts. It constructs a least-squares fit of the two GW polarizations to the data from the different detectors using the constraint likelihood method [27]. The cWB algorithm was first used in search for gravitational wave bursts in the LIGO-GEO network [42]. More recently it has been used in the LIGO S5 first-year low-frequency search [12], and detailed descriptions of the algorithm can be found there and in [26,27].

The cWB analysis in this search covers frequencies from 64 Hz to 6.0 kHz, with the data processing split into two bands. The low-frequency (LF) band (64 Hz to 2.0 kHz) contains the most sensitive (but also the most nonstationary) data. The high-frequency (HF) band (1.28 kHz to 6.0 kHz) is dominated by the shot noise of the detectors and is much less polluted by environmental and instrumental transients. Splitting the analysis into two bands is convenient for addressing the different noise characteristics in these bands. It also eases the computational cost. The overlap of the bands is used to cross-check the results and to preserve the sensitivity to wide-band signals near the boundary between the bands.

The cWB analysis is performed in several steps. First, the data are decomposed into Meyer wavelets. Time-frequency resolutions of ($8 \times 1/16$, $16 \times 1/32$, $32 \times 1/64$, $64 \times 1/128$, $128 \times 1/256$, $256 \times 1/512$ [Hz $\times$ s]) are used for the low-frequency search and ($12.5 \times 1/25$, $25 \times 1/50$, $50 \times 1/100$, $100 \times 1/200$, $200 \times 1/400$, $400 \times 1/800$ [Hz $\times$ s]) for the high-frequency search. The data are processed with a linear predictor error filter to remove power lines, violin modes and other predictable data components. Triggers are identified as sets of wavelet pixels among the detectors containing excess power at time delays consistent with a gravitational wave from a physical sky position. For each trigger, trial incoming sky locations are sampled with 1° resolution, and various coherent statistics are computed. These include the maximum likelihood ratio L_m (a measure of the sum-squared matched-filter SNR detected in the network), the network correlated amplitude η, the network correlation coefficient (cc), the

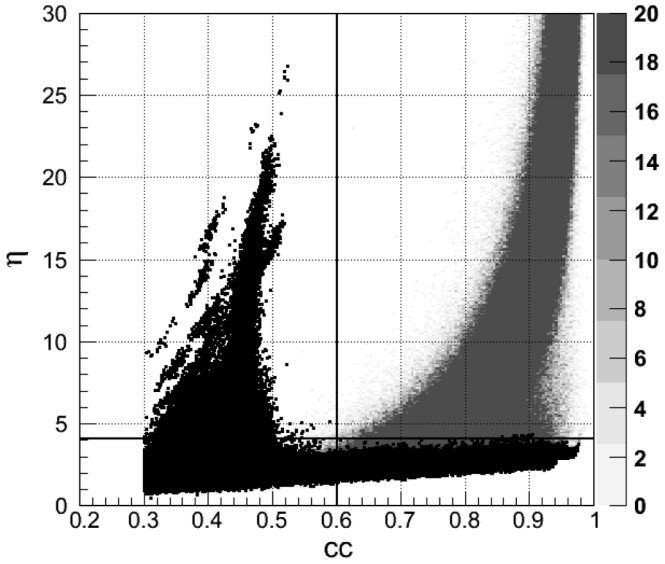

FIG. 9. Distribution of background triggers (black dots) after category 2 DQFs and vetoes for the L1H1H2 network for the high-frequency search, with $Q = 9$ sine-Gaussians injections (gray dots). The dashed lines show the thresholds on η and cc chosen for this network.

TABLE VII. Thresholds for each network for the cWB low- and high-frequency searches. Different thresholds on η are used for triggers below 200 Hz (η_1) and above 200 Hz (η_2) due to the different characteristics of the LIGO background noise in these frequency ranges. No energy disbalance cuts (Λ_{NET}, Λ_{HH}) are applied in the high-frequency search. In addition, a penalty factor cut of $P_f > 0.6$ is applied to all network configurations and searches.

	cWB LF						cWB HF		
	cc	η_1	η_2	Λ_{HH}	Λ_{NET}	P_f	cc	η	P_f
H1H2L1V1	0.5	4.5	4.1	0.3	0.35	0.6	0.6	4.3	0.6
H1H2L1	0.6	6.0	4.2	0.3	0.35	0.6	0.6	4.1	0.6
H1H2V1	...	...	...	...	...	...	0.7	4.6	0.6
H1L1V1	0.5	5.0	5.0	...	0.7	0.6	0.6	6.0	0.6
H1H2	0.6	6.0	4.1	0.3	0.35	0.6	0.5	5.0	0.6
H1L1	0.6	9.0	5.5	...	0.35	0.6	...	...	...
H2L1	0.6	6.5	5.5	...	0.35	0.6	...	...	...

energy disbalance statistics Λ, Λ_{HH} and the penalty factor P_f. (Each of these statistics is described in detail in [12].) The trial sky position giving the largest $cc \cdot L_m$ is selected as the best-guess incident direction, and the coherent statistics for this position are recorded. Finally, several post-production selection cuts are applied to the triggers to reduce the background.

Two groups of selection cuts are used in cWB. First, cuts on cc, Λ, Λ_{HH} and P_f are used to distinguish noise outliers from genuine GW signals. The most powerful consistency cut is based on the network correlation coefficient cc. For example, Fig. 9 shows a scatter plot of background triggers as a function of η and cc. Strong outliers (with large values of η) are characterized by low values of cc and are well separated from simulated signals. Additional selection cuts are based on the energy disbalance statistics Λ_{NET}, Λ_{HH}, and P_f. They are used to reject specific types of background events, such as H1-H2 correlated transients.

The second, final cut is on the network correlated amplitude η, which characterizes the significance of the triggers. Because of different characteristics of the background noise during the run and in the different frequency bands, the threshold on η is selected separately for each network configuration and frequency band to give false alarm probabilities of a few percent. In particular, in the low-frequency search separate η thresholds are used for triggers below and above 200 Hz. Table VII shows the thresholds used in the analysis.

The background is estimated separately on each segment of data processed. The cWB algorithm forms circular data buffers and shifts one detector with respect to the others, repeating the analysis hundreds of times on the time-shifted data. Table VIII shows the number of lags and accumulated background observation time for the various cWB searches and network configurations. The background data sets are used for tuning of the cWB selection cuts and also for estimation of the significance of the foreground events. For example, to estimate the significance of the blind injection identified by cWB, we generated a background sample with observation time equivalent to approximately 1000 H1H2L1 S5y2/VSR1 data sets.

TABLE VIII. Background observation time and false alarm rates for each network for the cWB low- and high-frequency searches.

	cWB LF Background			cWB HF Background		
	# lags	Obs time [year]	FAR year^{-1}	# lags	Obs time [year]	FAR year^{-1}
H1H2L1V1	200	34.8	0.3	96	17.6	0.17
H1H2L1	1000	499.9	0.1	96	31.7	0.09
H1H2V1	...	...	...	96	3.7	0.27
H1L1V1	200	1.8	3.3	288	3.0	0.33
H1H2	200	28.2	0.04	192	17.2	0.06
H1L1	200	4.6	2.0	...	...	...
H2L1	200	1.6	0.6	...	...	...

[1] C. Cutler and K. S. Thorne, in *Proc. of GR16*, edited by N. T. Bishop and S. D. Maharaj (World Scientific, Singapore, 2002).

[2] F. Pretorius, in *Physics of Relativistic Objects in Compact Binaries: from Birth to Coalescence*, edited by M. Colpi *et al.* (Springer Verlag, Berlin, 2009).

[3] Z. B. Etienne *et al.*, Phys. Rev. D **77**, 084002 (2008).

[4] C. D. Ott, Classical Quantum Gravity **26**, 063001 (2009).

[5] L. Baiotti *et al.*, Classical Quantum Gravity **24**, S187 (2007).

[6] S. Mereghetti, Astron. Astrophys. Rev. **15**, 225 (2008).

[7] N. Andersson and G. L. Comer, Phys. Rev. Lett. **87**, 241101 (2001).

[8] T. Damour and A. Vilenkin, Phys. Rev. D **64**, 064008 (2001).

[9] B. P. Abbott *et al.*, Rep. Prog. Phys. **72**, 076901 (2009).

[10] H. Grote (for the LIGO Scientific Collaboration), Classical Quantum Gravity **25**, 114043 (2008).

[11] F. Acernese *et al.*, Classical Quantum Gravity **25**, 114045 (2008).

[12] B. P. Abbott *et al.*, Phys. Rev. D **80**, 102001 (2009).

[13] B. P. Abbott *et al.*, Phys. Rev. D **80**, 102002 (2009).

[14] P. Astone *et al.*, Phys. Rev. D **68**, 022001 (2003).

[15] P. Astone *et al.*, Phys. Rev. D **76**, 102001 (2007).

[16] B. Alessandro, C. Beatrice, G. Bertotti, and A. Montorsi, J. Appl. Phys. **68**, 2908 (1990).

[17] S. Braccini *et al.*, Astropart. Phys. **23**, 557 (2005).

[18] This search includes several hours of data collected on 1 October 2007, after the official end of the S5 and VSR1 runs at 0:00 UTC on that day.

[19] For reference, a list of all time intervals included in the search may be found at https://dcc.ligo.org/cgi-bin/DocDB/ShowDocument?docid=T1000099&version=1.

[20] W. G. Anderson, P. R. Brady, J. D. Creighton, and É. É. Flanagan, Phys. Rev. D **63**, 042003 (2001).

[21] S. K. Chatterji, Ph.D. thesis, Massachusetts Institute of Technology, 2005.

[22] J. W. C. McNabb *et al.*, Classical Quantum Gravity **21**, S1705 (2004).

[23] S. Klimenko, I. Yakushin, M. Rakhmanov, and G. Mitselmakher, Classical Quantum Gravity **21**, S1685 (2004).

[24] F. Beauville *et al.*, Classical Quantum Gravity **25**, 045002 (2008).

[25] S. Chatterji, L. Blackburn, G. Martin, and E. Katsavounidis, Classical Quantum Gravity **21**, S1809 (2004).

[26] S. Klimenko *et al.*, Classical Quantum Gravity **25**, 114029 (2008).

[27] S. Klimenko, S. Mohanty, M. Rakhmanov, and G. Mitselmakher, Phys. Rev. D **72**, 122002 (2005).

[28] O. Benhar, V. Ferrari, and L. Gualtieri, Phys. Rev. D **70**, 124015 (2004).

[29] P. J. Sutton, Classical Quantum Gravity **26**, 245007 (2009).

[30] B. Abbott *et al.*, Classical Quantum Gravity **24**, 5343 (2007).

[31] B. Abbott *et al.*, Phys. Rev. D **72**, 062001 (2005).

[32] C. D. Ott, A. Burrows, L. Dessart, and E. Livne, Phys. Rev. Lett. **96**, 201102 (2006).

[33] L. Blackburn *et al.*, Classical Quantum Gravity **25**, 184004 (2008).

[34] N. Leroy *et al.*, Classical Quantum Gravity **26**, 204007 (2009).

[35] L. Blackburn *et al.* Report No. LIGO-G050158-00-Z, 2005, http://www.ligo.caltech.edu/docs/G/G050158-00.

[36] T. Ballinger *et al.*, Classical Quantum Gravity **26**, 204003 (2009).

[37] A. C. Clapson *et al.*, Classical Quantum Gravity **25**, 035002 (2008).

[38] F. Acernese *et al.*, Classical Quantum Gravity **26**, 085009 (2009).

[39] N. Arnaud *et al.*, Phys. Rev. D **67**, 102003 (2003).

[40] J. Makhoul, Proc. IEEE **63**, 561 (1975).

[41] This statement is actually only approximately correct due to complications related to normalization. See [12] for more details.

[42] B. Abbott *et al.*, Classical Quantum Gravity **25**, 245008 (2008).